

REPORT DOCUMENTATION PAGE

Form Approved OMB No. 0704-0188

Public reporting burden for this collection of information is estimated to average 1 hour per response, including the time for reviewing instructions, searching existing data sources, gathering and maintaining the data needed, and completing and reviewing the collection of information. Send comments regarding this burden estimate or any other aspect of this collection of information, including suggestions for reducing the burden, to Department of Defense, Washington Headquarters Services, Directorate for Information Operations and Reports (0704-0188), 1215 Jefferson Davis Highway, Suite 1204, Arlington, VA 22202-4302. Respondents should be aware that notwithstanding any other provision of law, no person shall be subject to any penalty for failing to comply with a collection of information if it does not display a currently valid OMB control number.
PLEASE DO NOT RETURN YOUR FORM TO THE ABOVE ADDRESS.

1. REPORT DATE (DD-MM-YYYY) 10-08-2005	2. REPORT TYPE Final Report	3. DATES COVERED (From – To) 1 July 2002 - 18-Jan-06
--	---------------------------------------	--

4. TITLE AND SUBTITLE Flow Structure Interaction on Flexible UCAV Wing Platforms	5a. CONTRACT NUMBER F61775-02-C4024
	5b. GRANT NUMBER
	5c. PROGRAM ELEMENT NUMBER

6. AUTHOR(S) Dr. Ismet Gursul	5d. PROJECT NUMBER
	5d. TASK NUMBER
	5e. WORK UNIT NUMBER

7. PERFORMING ORGANIZATION NAME(S) AND ADDRESS(ES) University of Bath Claverton Down Bath BA2 7AY United Kingdom	8. PERFORMING ORGANIZATION REPORT NUMBER N/A
---	--

9. SPONSORING/MONITORING AGENCY NAME(S) AND ADDRESS(ES) EOARD PSC 802 BOX 14 FPO 09499-0014	10. SPONSOR/MONITOR'S ACRONYM(S)
	11. SPONSOR/MONITOR'S REPORT NUMBER(S) SPC 02-4024

12. DISTRIBUTION/AVAILABILITY STATEMENT
Approved for public release; distribution is unlimited.

13. SUPPLEMENTARY NOTES

14. ABSTRACT

This report results from a contract tasking University of Bath as follows: The next generation of unpiloted combat air vehicles (UCAV's) will likely have flexible delta wings and will likely need the capability to perform extreme maneuvers at high g's. Vortical flows over delta wings produce periodic aerodynamic excitation which may cause unacceptable buffeting of a flexible wing structure. In this effort the contractor will investigate unsteady vortex flows over flexible delta wings, their interaction with the wing, and possibility of flow control by structural tuning. Basic research issues related to fluid/structure interactions for vortical flows will be addressed in analytical modeling, water tunnel testing, and wind tunnel testing. Wingtip accelerations will be measured using multiple accelerometers. PIV and LDV measurements will be used to capture the steady and unsteady phenomena in the wing flow field. The model geometry of the delta wing is simple, hence the experimental results may serve as benchmark tests for computational simulations.

15. SUBJECT TERMS
EOARD, Aerodynamics, Aeroelasticity, UCAVs

16. SECURITY CLASSIFICATION OF:			17. LIMITATION OF ABSTRACT UL	18. NUMBER OF PAGES 51	19a. NAME OF RESPONSIBLE PERSON SURYA SURAMPUDI
a. REPORT UNCLAS	b. ABSTRACT UNCLAS	c. THIS PAGE UNCLAS			19b. TELEPHONE NUMBER (Include area code) +44 (0)20 7514 4299

**FLOW STRUCTURE INTERACTION ON FLEXIBLE UCAV
WING PLATFORMS**

Contract No: F61775-02-C4024

Final Report

Months 31-36

submitted to

**Dr. Surya Surampudi
European Office of Aerospace Research & Development (EOARD)
223/231 Old Marylebone Road
NW1 5TH London, UK**

by

**Professor Ismet Gursul
Department of Mechanical Engineering
University of Bath
Bath, BA2 7AY
United Kingdom**

June 2005

CONTENTS

1. SUMMARY
2. MAIN FINDINGS (last six months)
3. APPENDIX 1: List of Publications from This Project
4. APPENDIX 2: AIAA-2005-0865, “Passive Flow Control over Flexible Nonslender Delta Wings”
5. APPENDIX 3: AIAA-2005-0867, “Physical Mechanisms of Lift Enhancement for Flexible Delta Wings”

1. SUMMARY

In the second half of the third year of the project, further experiments have been conducted in several areas. These include detailed PIV and LDV measurements of the vortical flow in the wind tunnel to provide high Reynolds number data for comparisons with the computational simulations (carried out by Dr. Ray Gordnier and Dr. Miguel Visbal, Computational Sciences Branch, Air Vehicles Directorate), hot-wire measurements for spectral analysis of unsteady flow features, as well as flow visualization for oscillating rigid wings in the water tunnel to study the effects of wing sweep angle and symmetric perturbations. In both the wind tunnel and water tunnel experiments, flow visualization, velocity measurements and force measurements provide insight to lift enhancement and flow reattachment over flexible and oscillating wings. A list of publications originated from this project and two recent conference papers are attached.

2. MAIN FINDINGS

2.1. Wind tunnel experiments

2.1.1. PIV and LDV measurements

The main objective of these measurements was to provide high Reynolds number data for the vortical flow before the stall ($\alpha=15^\circ$). These data have been used for comparisons with the computational simulations. Figure 1 shows the PIV data from the wind tunnel experiments and also compares with the water tunnel experiments. There are

strong similarities, although some differences in the breakdown location and the spanwise location of the vortex exist. LDV measurements provide higher resolution and also provide information on the rms velocity. An example is shown in Figure 2. Detailed results (not shown here) were provided to our collaborators in the AFRL.

2.1.2. Spectral analysis

Both LDV and hot-wire measurements were conducted for spectral analysis of unsteady flow features. The data rate of the LDV data was not sufficiently high for this purpose. Therefore, extensive measurements were taken with a single hot wire, and also with two hot-wires (for simultaneous measurements). Figure 3 shows the spectra of velocity fluctuations at different spanwise locations for the rigid wing, $\alpha=20^\circ$, $x/c=0.7$. For this angle of attack, vortex breakdown is already at the apex of the wing. It is seen that a broad peak exists in the spectra, and also the center frequency is approximately the same. As the locations of measurements are close to the separated shear layer, it is believed that these peaks correspond to the dominant frequency of the shear layer structures.

Figure 4 shows the effect of streamwise distance on the spectra of velocity fluctuations for $\alpha=20^\circ$. It is seen that the center peaks decrease with increasing streamwise distance. Figure 5 shows the spectra for various angles of attack in the range of $\alpha=5^\circ$ to $\alpha=25^\circ$ for the rigid wing. The dominant peaks are seen for $\alpha \geq 15^\circ$, which covers the flow regimes when vortex breakdown exist over the wing as well as stalled flow. Hence, it is believed that these are due to the shear layer instabilities, although there is the possibility that vortex breakdown might be driving these instabilities at lower incidences.

Simultaneous measurements at two locations, which are the mirror images, indicated that there was no coherence between the two signals as shown in Figure 6. This was somewhat surprising in that the dominant peaks observed in the spectra are not correlated at all for the rigid wing. When similar measurements were carried out for the flexible wing, the large sharp peak corresponding to the wing vibrations is seen in the spectrum of velocity fluctuations in Figure 7 in the post-stall region. Figure 8 shows the

amplitude and phase of the coherence between the two velocity signals, which confirm the anti-symmetric nature of the oscillations.

2.2. Water tunnel experiments

2.2.1. Laser fluorescence flow visualization for oscillating wings

Experiments with a rigid wing undergoing small-amplitude rolling motion were conducted in order to simulate the effect of antisymmetric vibrations. In these experiments, fluorescent dye was released from a slot near the leading-edge, hence it “marks” the vorticity shed with separation. The objective was to visualize the shear layer structures.

Figure 9 shows flow visualization for the stationary and rolling delta wing (with an amplitude of 1° and $St=1.0$) for angles of attack of $\alpha=15^\circ$, $\alpha=20^\circ$ and $\alpha=25^\circ$ at $x/c=0.8$. While the difference is small for $\alpha=15^\circ$, the change in the size of the separation region is considerable for the oscillating wing due to earlier reattachment. The wavelength of the vortical structures on stationary and oscillating wing suggests that the natural frequency of the shear layer instability is close to $St=1$, which is also close to the center peak frequency of the hot-wire measurements. Recall that this also corresponds to an “optimum frequency” for which breakdown location is delayed to a maximum distance from the apex. Figure 10 shows the time-averaged flow visualization for the three incidences.

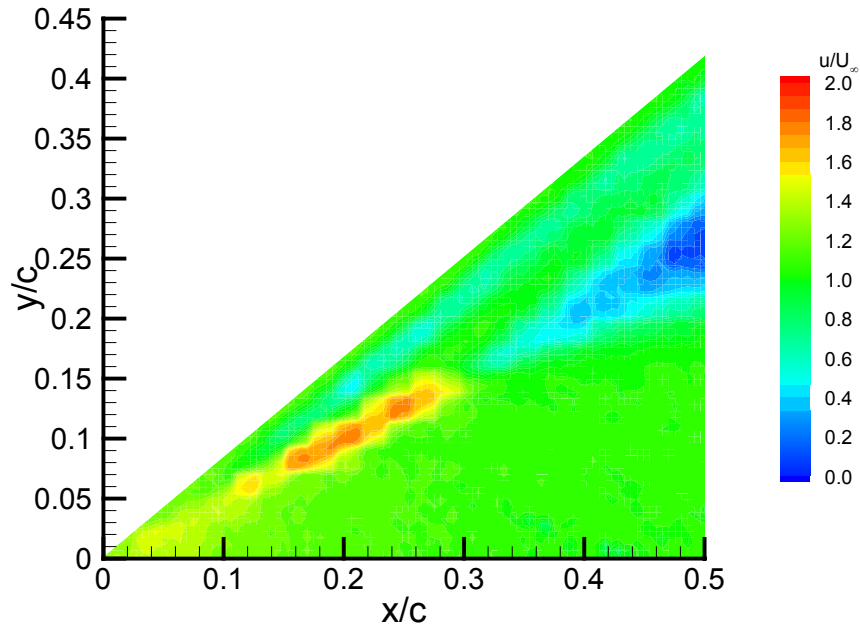
2.2.2. Effect of wing sweep

Figure 11 and 12 show flow visualization pictures for $\Lambda=40^\circ$ and $\Lambda=30^\circ$ wings at various post-stall angles of attack for stationary and oscillating cases. It is seen that in all cases flow reattachment occurs over the wing for the roll oscillations at $St=1.0$. Although not shown here, detailed examination and measurement of reattachment region showed that $St=1$ is around the “optimum” frequency, which is similar to $\Lambda=50^\circ$ wing results.

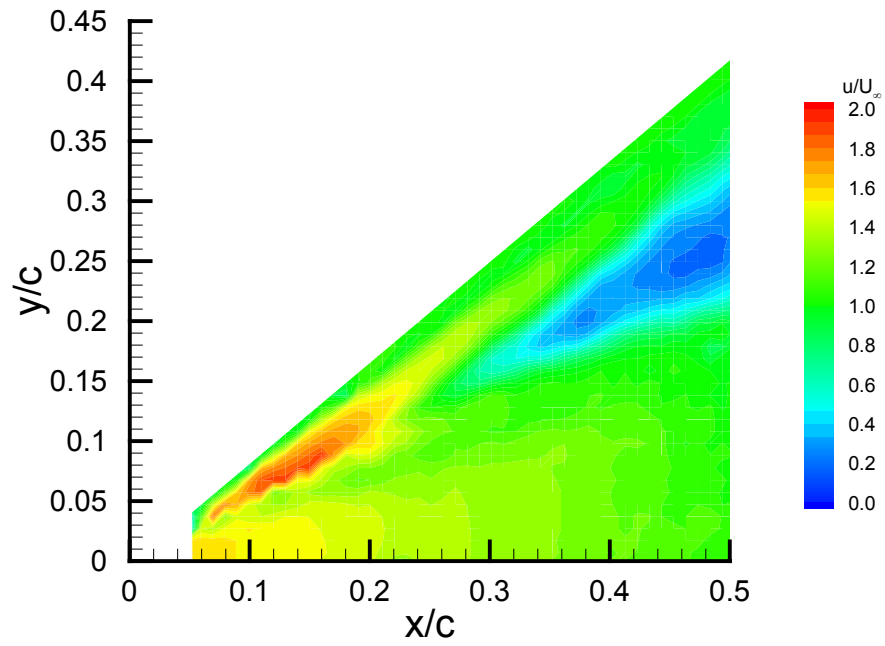
2.2.3. Symmetric oscillations

Effect of symmetric perturbations in the form of small amplitude pitching oscillations (1° amplitude) were studied. The results of flow visualization are shown in

Figure 13. Again, earlier reattachment and even the re-formation of the leading-edge vortex is observed for the oscillating wing. Hence, for active control purposes, both symmetric and anti-symmetric forcing would work. However, passive control for a flexible wing occurs only in the anti-symmetric mode.



(a) $\alpha = 15^\circ$, $\phi = 9^\circ$, $Re_c = 26,000$, Water-tunnel.



(b) $\alpha = 15^\circ$, $\phi = 10^\circ$, $Re_c = 620,000$, Wind-tunnel.

Figure 1: Comparison of PIV measurements for wind and water tunnel experiments.

Horizontal traverse at $x/c=20\%$, $\alpha=15^\circ$, $z/s=0.17$

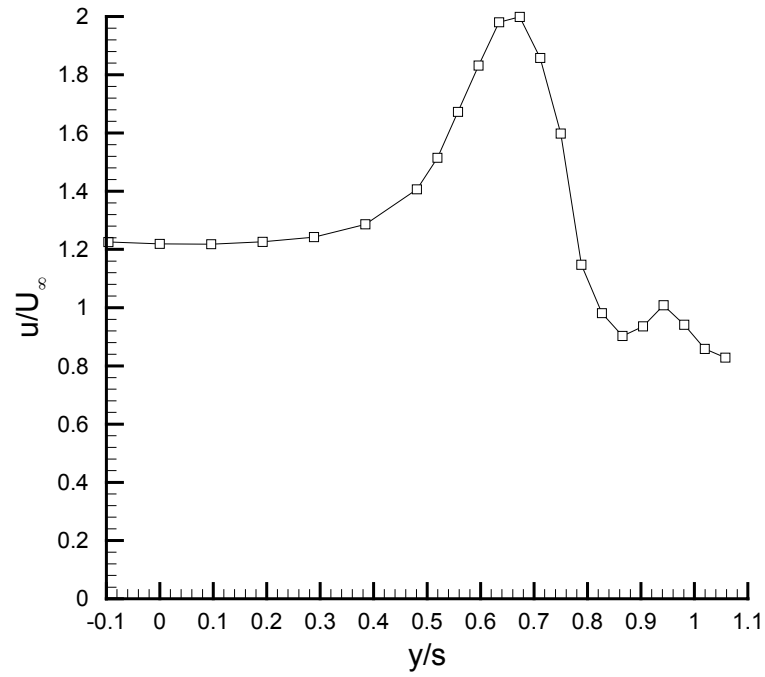


Figure 2: LDV measurements of velocity profile upstream of breakdown for $\alpha=15^\circ$.

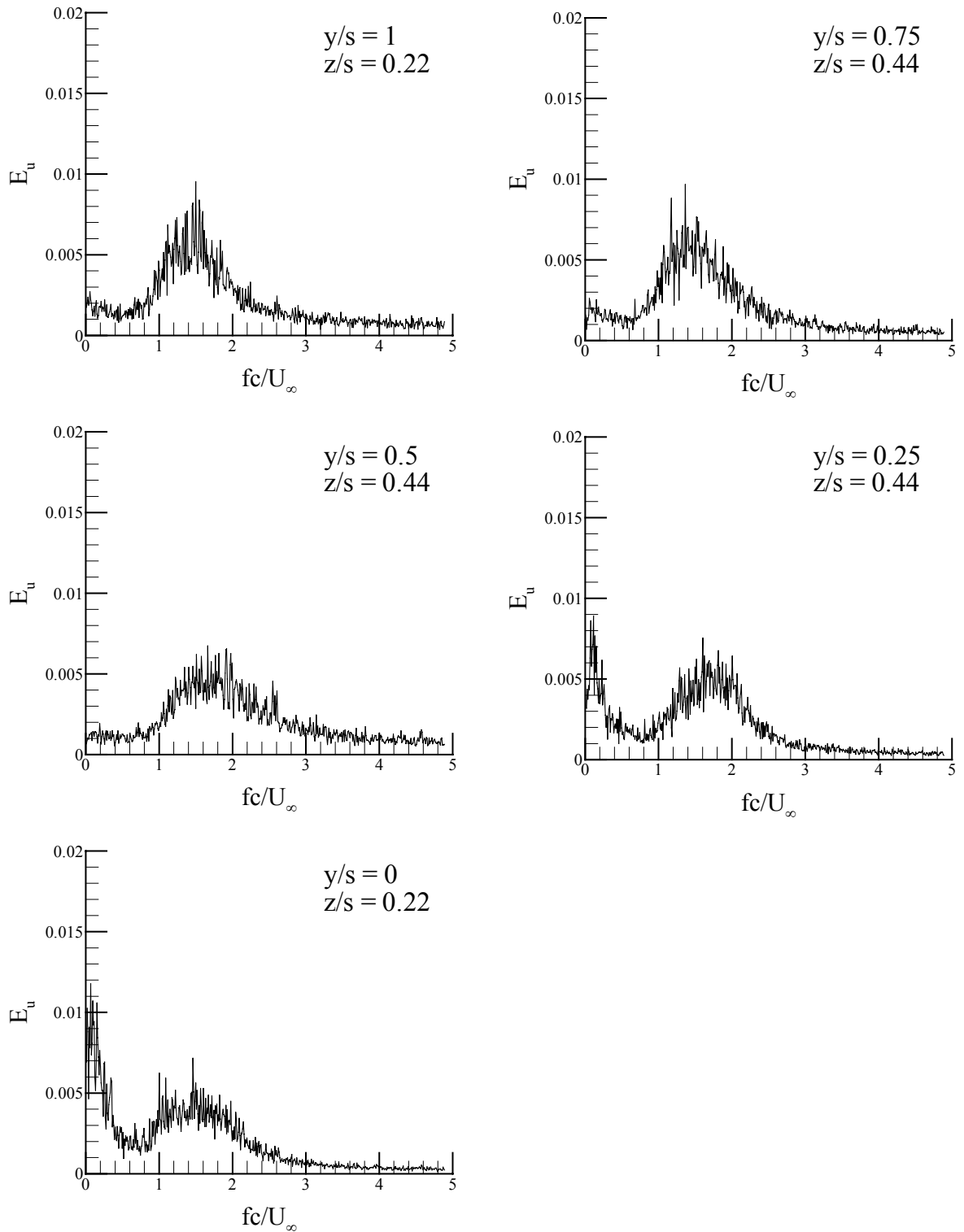


Figure 3: Effect of spanwise location on the spectra of velocity fluctuations for $\Lambda = 50^\circ$ rigid wing, $\alpha = 20^\circ$, $x/c=0.7$.

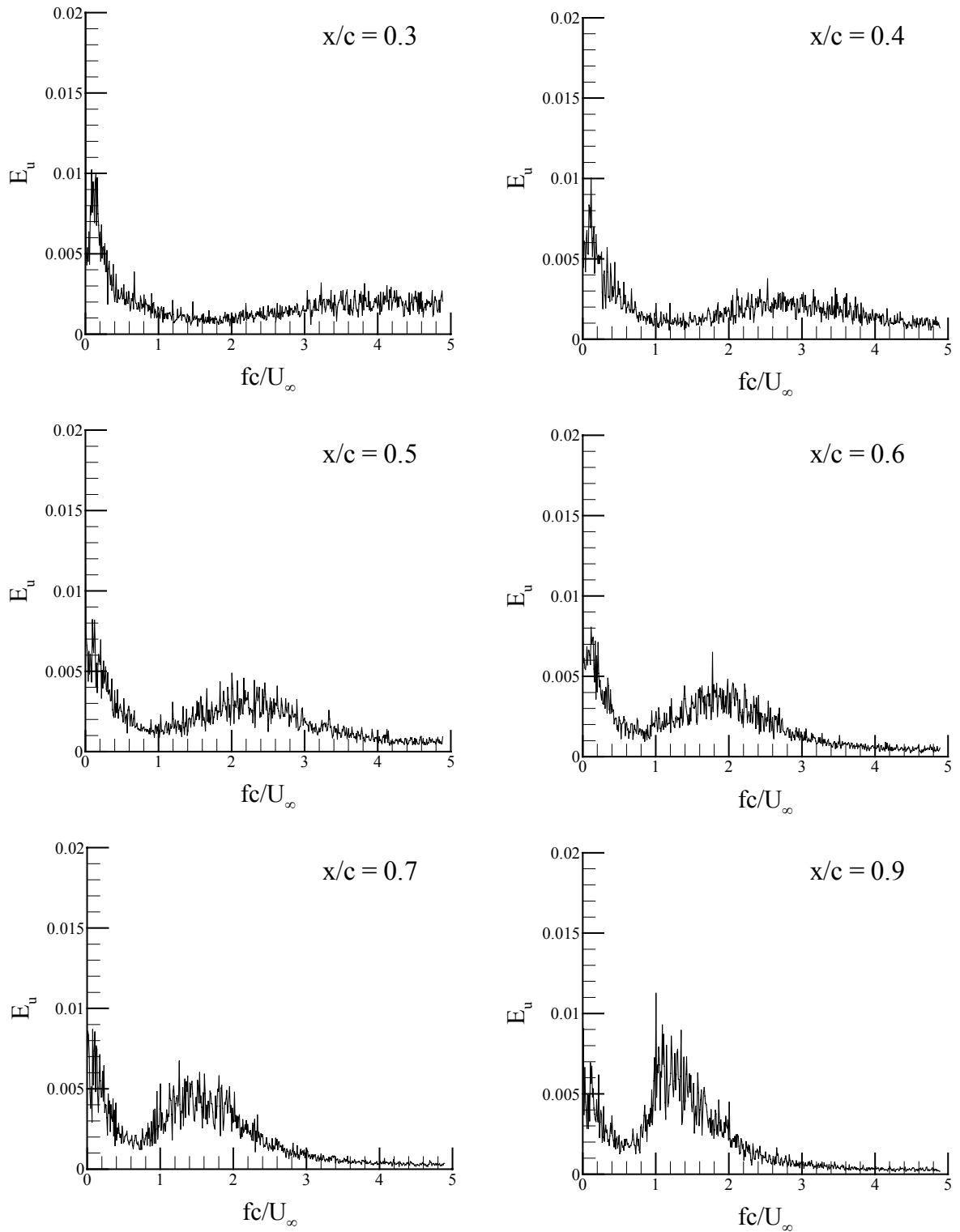


Figure 4: Effect of streamwise location on the spectra of velocity fluctuations for $\Lambda = 50^\circ$ rigid wing, $\alpha = 20^\circ$, $y/s = 0$, $z/s = 0.06$.

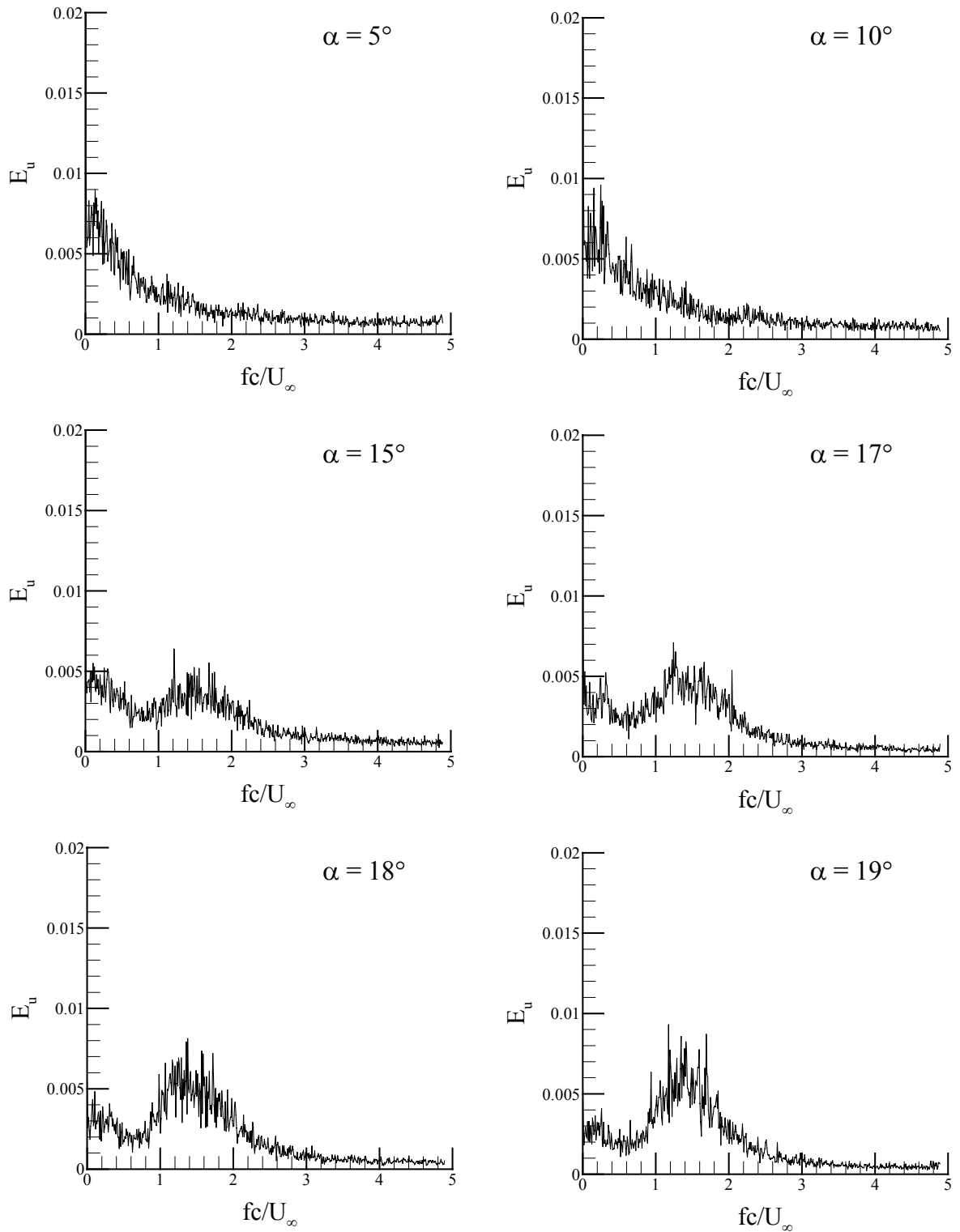


Figure 5: Effect of angle of attack on the spectra of velocity fluctuations for $\Lambda = 50^\circ$ rigid wing, $x/c = 0.7$, $y/s = 0.75$, $z/s = 0.44$.

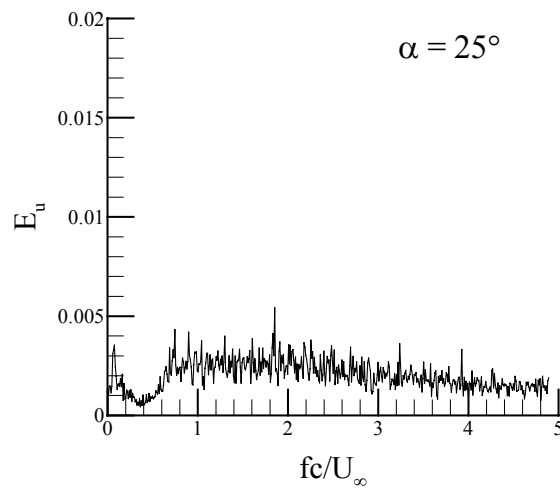
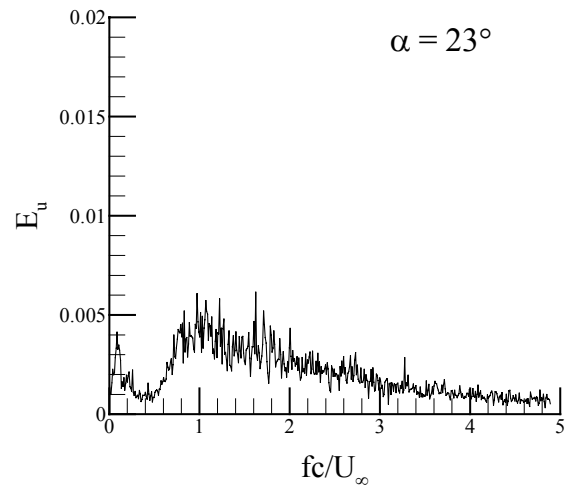
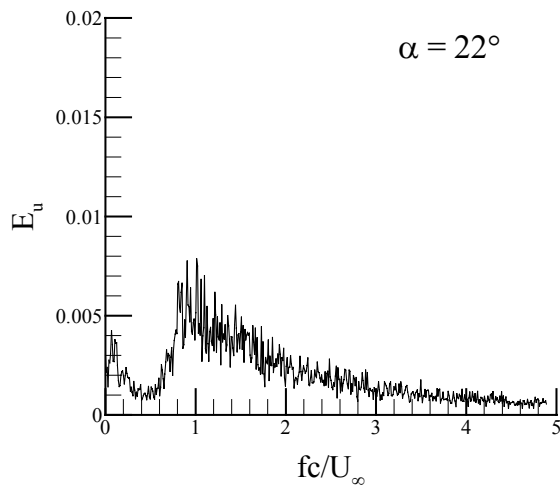
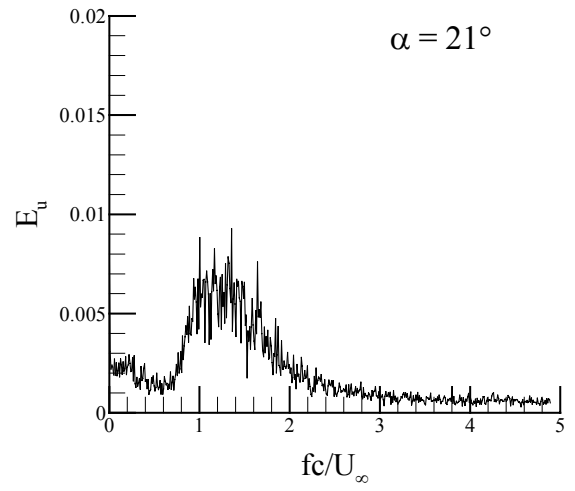
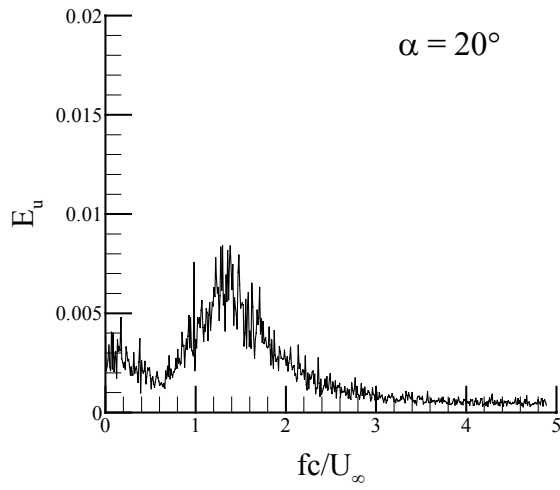


Figure 5: (Continued)

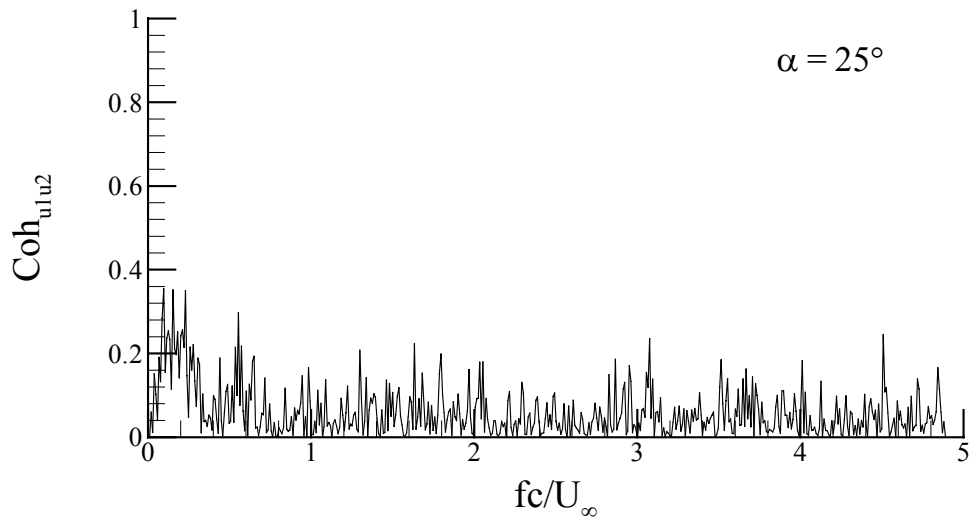
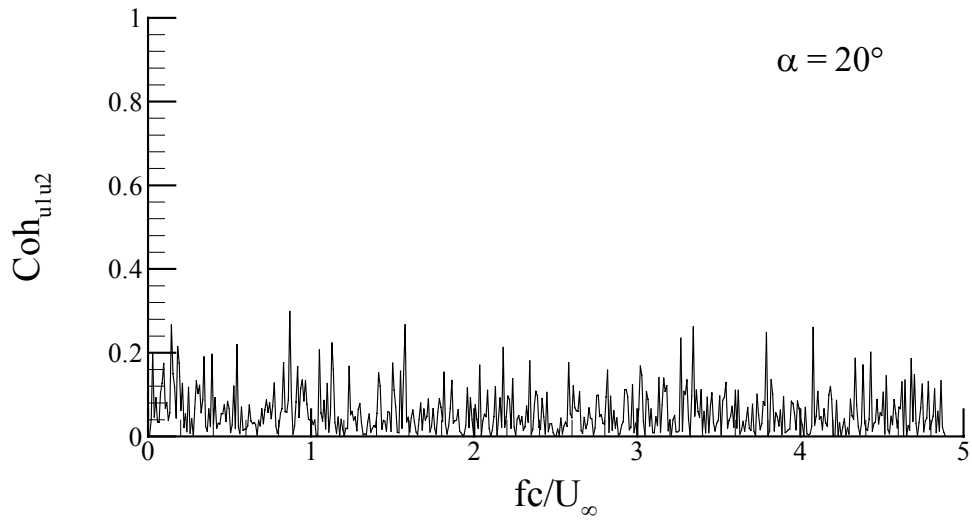
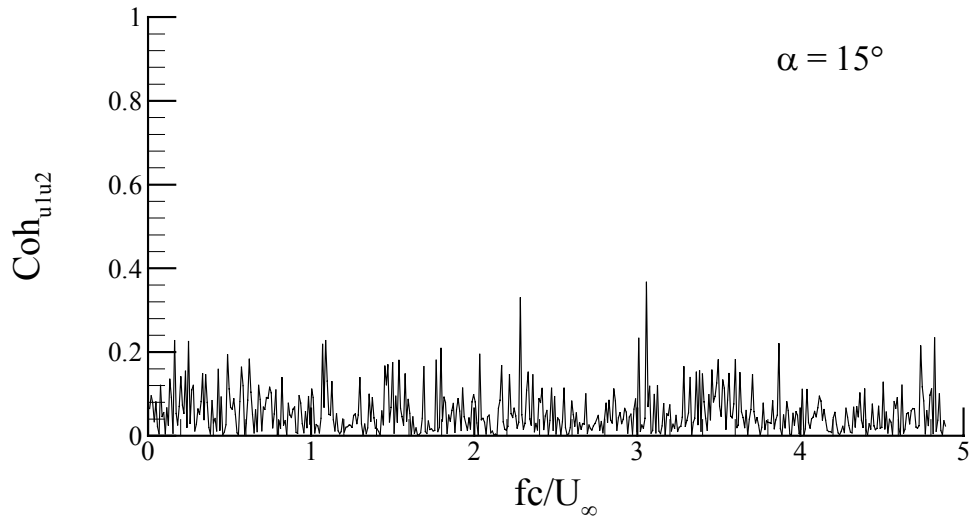


Figure 6: Coherence between the two velocity signals for $\Lambda = 50^\circ$ rigid wing, $x/c = 0.7$, $y/s = \pm 0.75$, $z/s = 0.44$

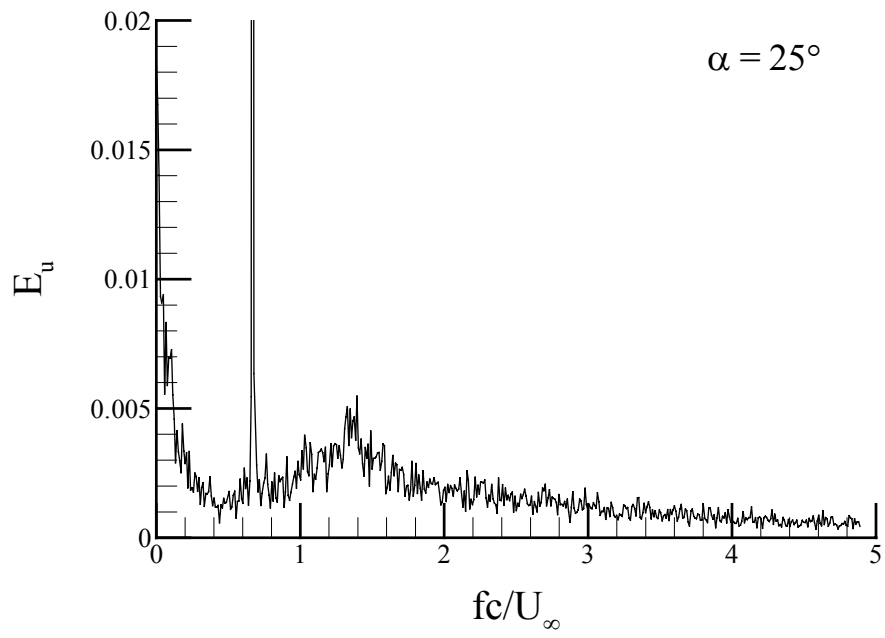


Figure 7: Spectrum of velocity fluctuations for $\Lambda = 50^\circ$ flexible wing, $x/c = 0.7$, $y/s = 0.25$, $z/s = 0.55$

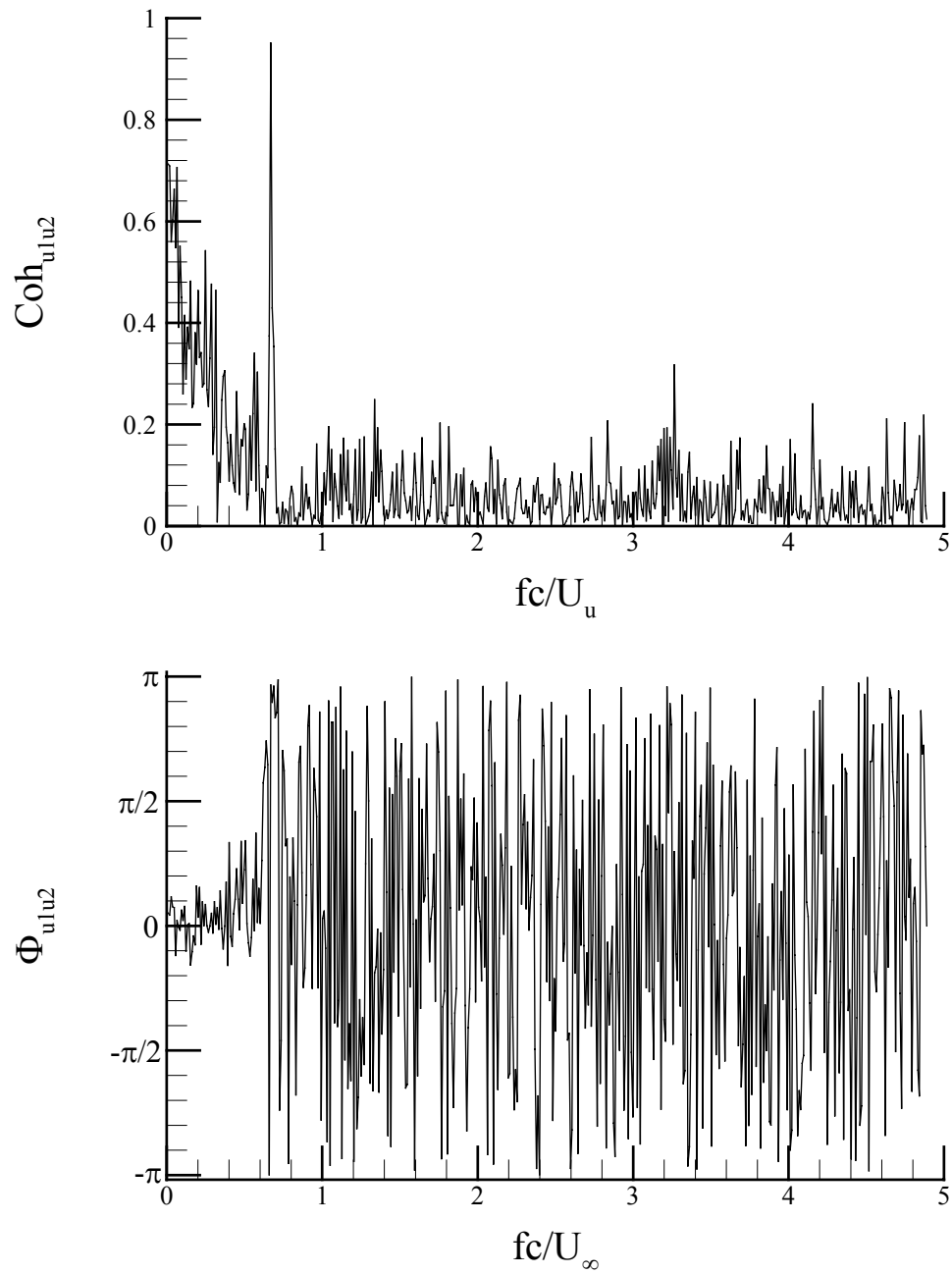
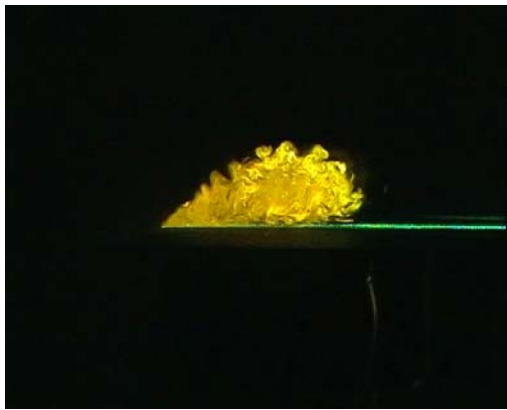


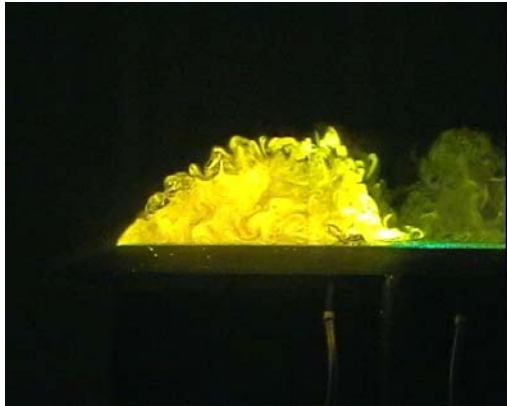
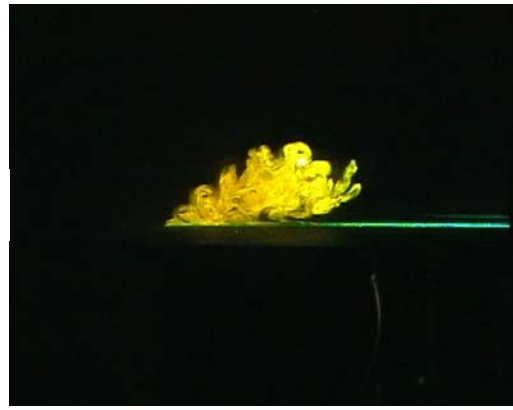
Figure 8: Amplitude and phase of coherence between the two velocity signals for $\Lambda = 50^\circ$ flexible wing, $\alpha = 25^\circ$, $x/c = 0.7$, $y/s = \pm 0.25$, $z/s = 0.55$

Stationary wing

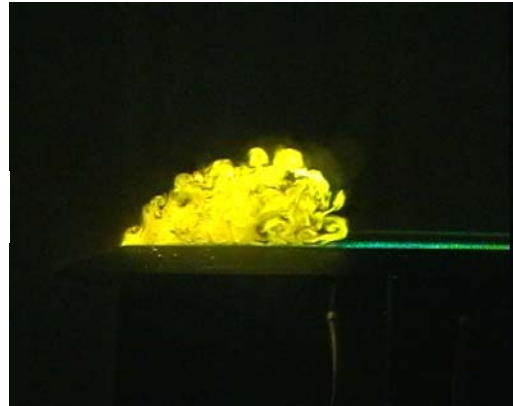
Oscillating wing



$\alpha=15^\circ$



$\alpha=20^\circ$



$\alpha=25^\circ$

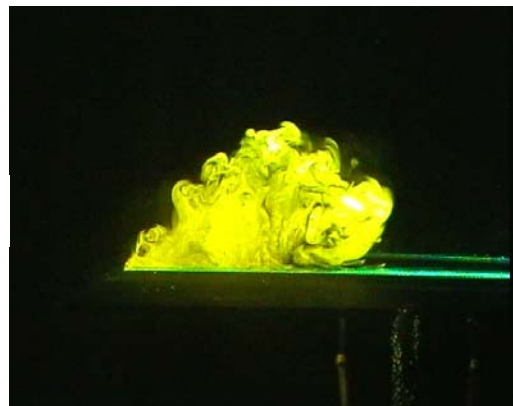
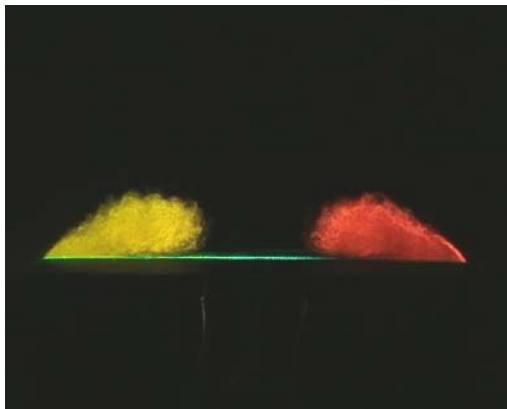


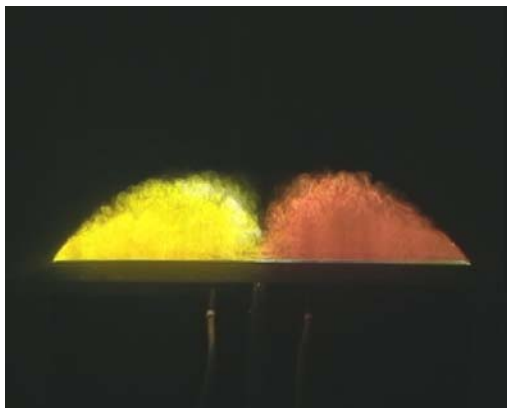
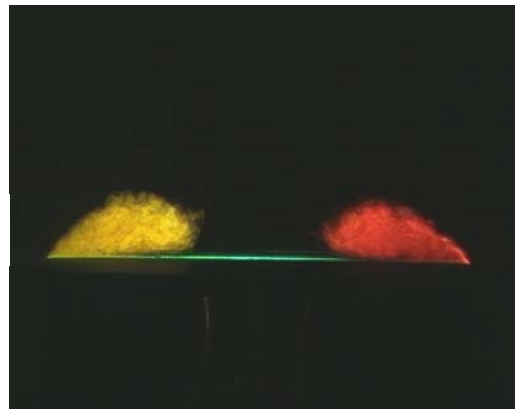
Figure 9: Laser fluorescence flow visualization for stationary and rolling wings ($St=1.0$, $\Delta\phi=1^\circ$).

Stationary wing

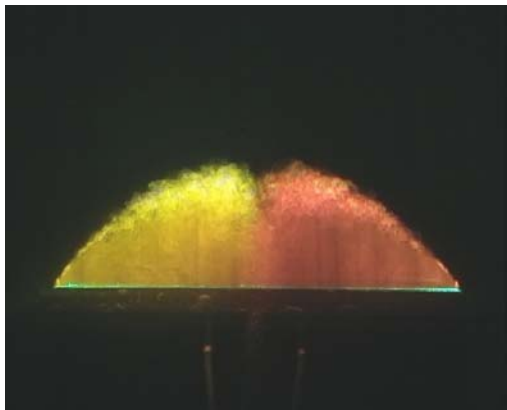
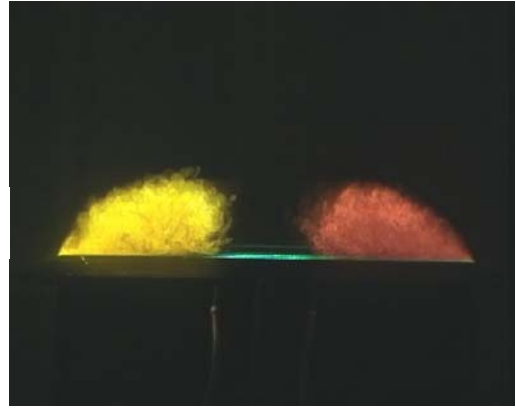
Oscillating wing



$\alpha=15^\circ$



$\alpha=20^\circ$



$\alpha=25^\circ$

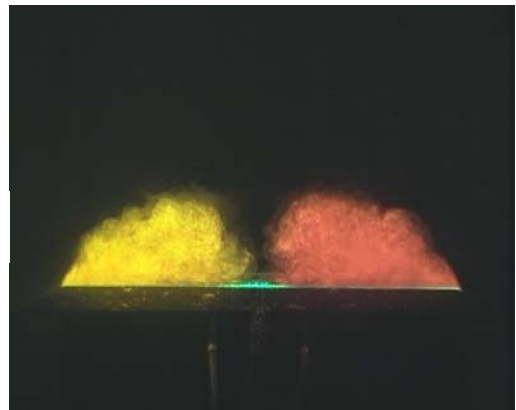
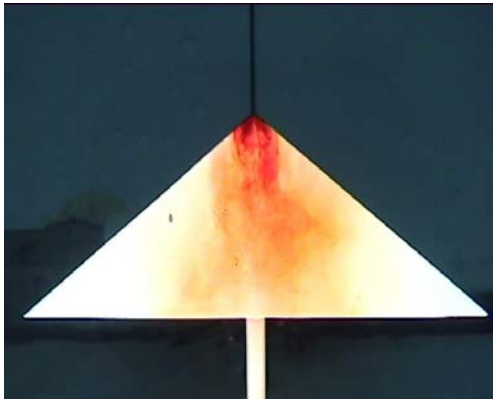


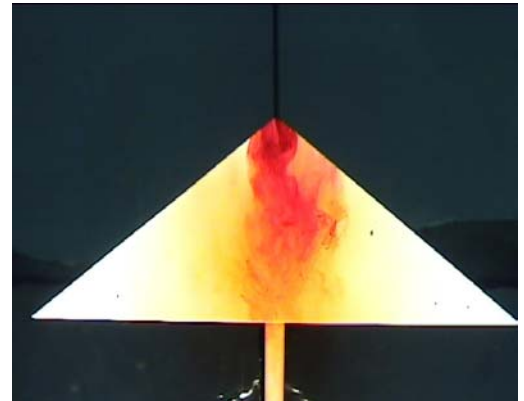
Figure 10: Time-averaged laser fluorescence flow visualization for stationary and rolling wings ($St=1.0$, $\Delta\phi=1^\circ$).

$\alpha = 20^\circ$



$fc/U_\infty = 0$

$\alpha = 25^\circ$



$fc/U_\infty = 1$

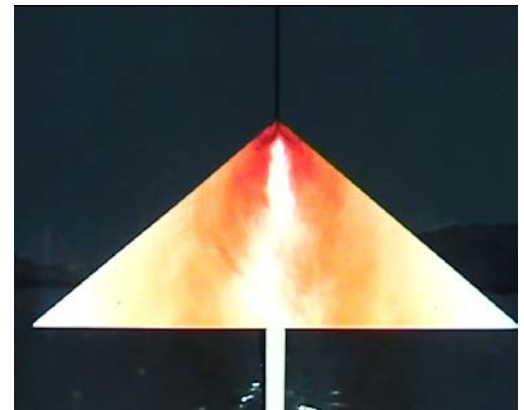
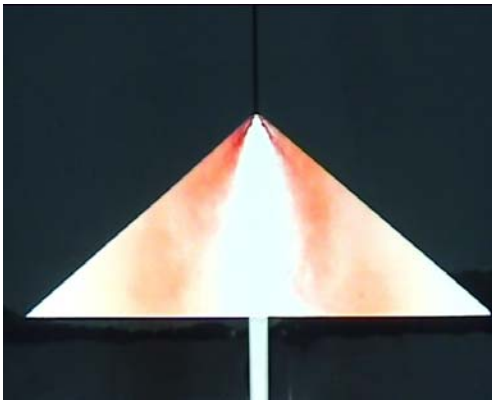


Figure 11: Wing sweep angle, $\Lambda=40^\circ$: flow visualization for stationary and oscillating wings in roll ($St=1.0$, $\Delta\phi=5^\circ$).

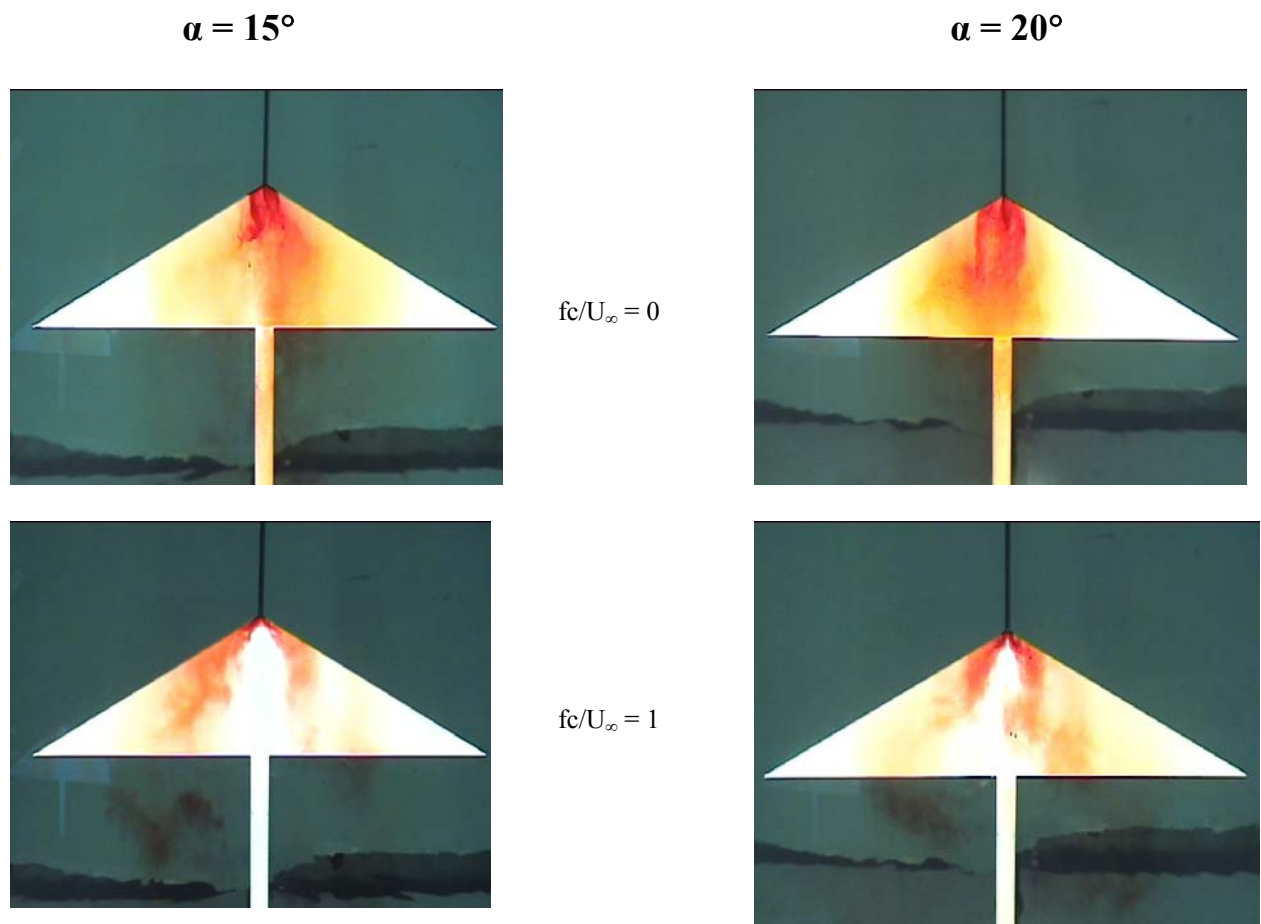
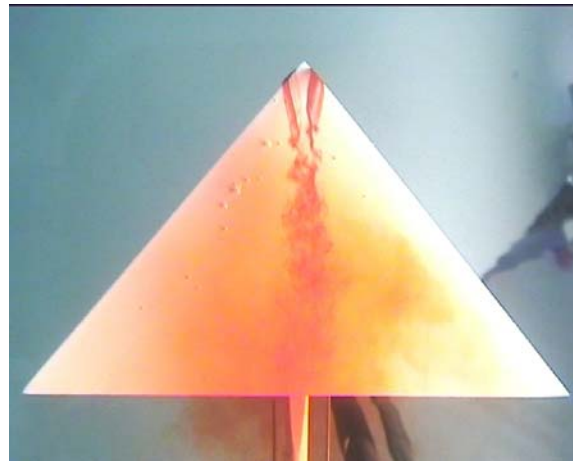
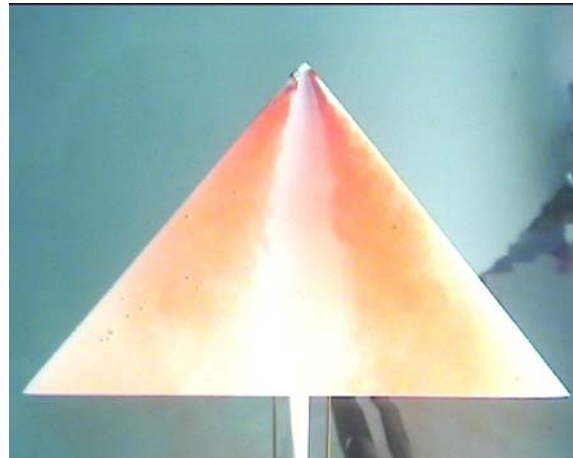


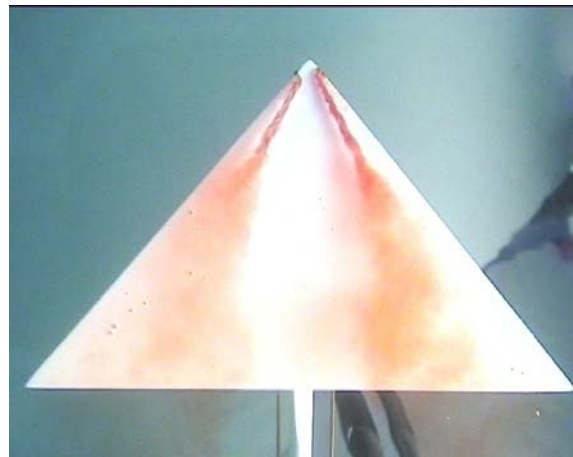
Figure 12: Wing sweep angle, $\Lambda=30^\circ$: flow visualization for stationary and oscillating wings in roll ($St=1.0$, $\Delta\phi=5^\circ$).



St = 0



St = 0.5



St = 1.19

Figure 13: Effect of symmetric (pitching) oscillations: flow visualization for stationary and oscillating wings ($St=1.0$, $\Delta\phi=1^\circ$, wing sweep angle $\Lambda=50^\circ$).

LIST OF PUBLICATIONS FROM THIS PROJECT

Journal publications:

TAYLOR, G. and GURSUL, I., “Buffeting Flows over a Low Sweep Delta Wing”, *AIAA Journal*, vol. 42, no. 9, September 2004, pp. 1737-1745.

GURSUL, I., GORDNIER, R. and VISBAL, M., “Unsteady Aerodynamics of Nonslender Delta Wings”, *Progress in Aerospace Sciences*, submitted for publication.

Conference Papers:

TAYLOR, G.S., SCHNORBUS, T. and GURSUL, I., 2003, “An Investigation of Vortex Flows over Low Sweep Delta Wings”, AIAA-2003-4021, AIAA Fluid Dynamics Conference, 23-26 June, Orlando, FL.

TAYLOR, G. and GURSUL, I., 2004, “Unsteady Vortex Flows and Buffeting of a Low Sweep Delta Wing”, AIAA-2004-1066, 42nd Aerospace Sciences Meeting and Exhibit, January 3-8, Reno, Nevada.

TAYLOR, G.S. and GURSUL, I., 2004, “Lift Enhancement over a Flexible Delta Wing”, AIAA-2004-2618, 2nd AIAA Flow Control Conference, June 2004, Portland.

VARDAKI, E., GURSUL, I. and TAYLOR, G., 2005, “Physical Mechanisms of Lift Enhancement for Flexible Delta Wings”, AIAA-2005-0867, 43rd Aerospace Sciences Meeting and Exhibit, 10-13 January 2005, Reno, NV.

TAYLOR, G.S., KROKER, A. and GURSUL, I., 2005, “Passive Flow Control over Flexible Nonslender Delta Wings”, AIAA-2005-0865, 43rd Aerospace Sciences Meeting and Exhibit, 10-13 January 2005, Reno, NV.

Passive Flow Control over Flexible Non-Slender Delta Wings

Gordon Taylor^{*}, Andreas Kroker[†] and Ismet Gursul[‡]

University of Bath, Bath, BA2 7AY, United Kingdom.

Force measurements over a range of non-slender delta wings have demonstrated the ability of a flexible wing to enhance lift and delay stall compared with a rigid wing of similar geometry. The work has extended the results of a recent study to include delta wings with a range of sweep angles. It has been shown that the greatest lift enhancement was observed over the wing with smallest leading edge sweep. Additionally for the only slender wing considered no lift enhancement was observed indicating that it is a feature of the fundamentally different flow that occurs over low-sweep wings that is responsible for the phenomenon. The variation of RMS lift force and rolling moment coefficients with incidence for all the wings concerned suggest that the wings are vibrating in an anti-symmetric structural mode in the lift enhancement region. This supports previous evidence for the 50° wing that suggests the same. Further, experiments of a half-wing model suggest that this wing does not undergo lift enhancement, and as such it may be that the anti-symmetric vibration is a necessary condition for the lift enhancement to exist. Wing-tip deflections for some of the wings were also measured, which showed that the slender wing undergoes much higher time-averaged deflections than the non-slender wings, although it also experiences a much lower level of buffet. PIV and LDV measurements have demonstrated the striking difference between the surface flows over the flexible and rigid wings in the post-stall region at the same incidence. Implementing flexibility on a low sweep wing results in continued reattachment of the shear layer to much higher incidences than would otherwise be observed over a rigid wing.

Nomenclature

c	=	root chord length
f	=	frequency
s	=	local semi-span
t	=	wing thickness
C_L	=	lift coefficient
C_R	=	Rolling moment coefficient
E	=	elastic modulus
Re	=	chord Reynolds number
St	=	Strouhal number ($= fc/U_\infty$)
U_∞	=	free-stream velocity
α	=	angle of attack
δ	=	wing-tip vertical deflection under load
λ_s	=	span-wise bending stiffness normalized by free-stream dynamic pressure ($= 12(1-\nu^2)\rho_\infty U_\infty^2 s^3/Et^3$)
ν	=	Poisson's ratio
ρ	=	density

^{*} Post-Doctoral Research Associate, Department of Mechanical Engineering, Member AIAA.

[†] Undergraduate Student, Department of Mechanical Engineering.

[‡] Professor of Aerospace Engineering, Department of Mechanical Engineering, Associate Fellow AIAA.

I. Introduction

The recent interest in Micro-Air-Vehicles (MAVs) and Unmanned-Air-Vehicles (UAVs) has resulted in a need to further our understanding of flows over non-slender delta wing configurations. While a non-slender wing may be out-performed by a slender wing in terms of maximum achievable lift and stall angle^{1,2,3}, the non-slender wing offers alternative advantages such as lower lift-to-drag ratio⁴ and a greater surface area allowing greater options for the internal packaging of flight systems, thus minimizing the impact on external aerodynamics. Both of these benefits are particularly important for small aircraft such as MAVs. For the purposes of this investigation, a non-slender wing is defined as one with leading edge sweep less than 60°. The flows that occur over non-slender wings have been shown to differ substantially from those documented over more slender planforms. While a slender wing produces a single coherent primary vortex from each leading edge, recent computational⁵ and experimental⁶ studies have demonstrated the existence of a ‘dual’ primary vortex structure over a non-slender wing. This vortex structure is a direct result of the proximity of the vortex formation to the wing surface^{7,8}, which results in significant interactions between the secondary and primary vortices. The primary vortex is split into two separate vortices by the secondary vortex, which occurs much further away from the primary vortex in slender wing flows. A further consequence of the interaction between the boundary layer and vortex flows is the sensitivity of non-slender wing flows to Reynolds number⁶ that is not observed over slender wings⁹. For $Re < 30,000$, decreasing Reynolds number results in a downstream movement of the vortex breakdown and a displacement of the vortex core towards the wing center-line⁶. The vortices generated over low sweep delta wing undergo breakdown at very low incidences⁶; for a 50° wing the breakdown has been observed over the upstream half of the wing at an incidence of just 2.5°. Detailed three-component PIV measurements have demonstrated the wake-like velocity profile of the leading edge vortices produced over a 50° wing¹⁰ at low Reynolds numbers. Further measurements have shown that this is a feature observed at low incidences¹¹, and is possibly a result of the propinquity of the vortices to the wing surface.

While the flows over non-slender wings have become a more popular topic in the literature over recent years, there have been few investigations of the effects of flexibility. An initial study into flexibility of a 60° wing showed that significant buffeting was present in the region just prior to the stall¹². For this wing, of thickness-to-chord ratio, $t/c = 0.44$, at a Reynolds number, $Re = O(10^6)$, finite element analysis complemented with wing-tip accelerometer measurements indicated that in this state the wing was vibrating in the second anti-symmetric structural mode¹². This was later confirmed with computational simulations, which showed significant peaks in the spectra of pressure fluctuations centered on the 2nd and 3rd modes of vibration¹³. Only recently have the effects of flexibility been studied for a non-slender delta wing. Studies of a 50° wing of thickness, $t/c = 0.65\%$ at a similar Reynolds number have also shown significant levels of buffet¹¹. There are a number of sources of unsteadiness that may manifest themselves as buffet, and these sources have been studied extensively over slender delta wings^{14,15}. It has been shown that for a slender wing the onset of breakdown forward of the trailing edge results in a sharp increase in the level of buffet, as measured by normal force fluctuations¹ and RMS wing-root strain¹⁶. Further, the onset of stall corresponds to a drop in the level of buffet¹², implying that the instabilities associated with the breakdown process are the dominating influence in the buffeting process over slender wings¹⁷. However, over non-slender wings, breakdown of the vortices has been observed over the wing at incidences as low as 2.5°, and breakdown can reach the apex at an incidence much lower than the stall angle⁶. In spite of this behavior, peak buffeting still occurs around the stall the angle over low-sweep wings¹¹, and instabilities associated with the shear layer reattachment process at high incidences have been proposed as the leading cause of buffet over these wings.

A recent study has documented a particularly interesting feature of non-slender wings of sufficient flexibility¹⁸. It was shown that for a wing of thickness, $t/c = 0.32\%$ at a Reynolds number, $Re = 6.2E5$, a region of significant lift enhancement exists in the range of incidences immediately following the stall. In this region, lift was shown to increase by 45% at $\alpha = 30^\circ$, and the stall may be delayed by up to 9°. Large wing tip deflections, both mean and fluctuating, were associated with the lift enhancement region, along with a switching of the dominant structural mode from the fundamental to the second anti-symmetric. The large time-averaged deflection was initially suspected as the cause, but comparison with wings with span-wise camber¹⁹ indicated that this should, if anything, result in a reduction in lift. Detailed measurements¹⁸ indicate that it was the magnitude of the tip vibrations that were responsible for this phenomenon.

The aim of this investigation was to study further the lift enhancement phenomenon that has been observed over non-slender delta wings. Specifically, the aims were to: (1) determine whether the same lift enhancement could be achieved over wings with leading edge sweep angles other than 50°; and (2) undertake measurements to document the flow structure in the lift enhancement region. These aims were achieved by complementing lift force data with near-surface PIV and off-surface LDV measurements.

II. Methodology

Wind tunnel experiments were conducted in the high speed working section of the 7' x 5' closed circuit facility at the University of Bath. Models were supported using the high-incidence mechanism as shown in Figure 1. Experiments were conducted at a free stream velocity of $U_\infty = 31.7$ m/s. Maximum blockage for the wind tunnel was approximately 2.3% for the 60° wing at $\alpha = 50^\circ$. Models of varying leading edge sweep and thickness were tested. Each model was a planar delta wing with a pressure surface leading edge bevel of 45°, and a square trailing edge. Figure 3 shows a schematic of the wing of 50° leading edge sweep; in addition to this, wings of 40°, 45°, 55°, and 60° sweep were tested. Each model had a semi-span, $s = 0.260$ m such that the span-wise flexural characteristics of the thin wings remained consistent between the models. Chord lengths, c , in the range 0.218 – 0.450 m were used resulting in chord Reynolds numbers in the range 440,000 – 900,000. Each model was made from aluminium alloy 1050A, which has the following material properties: $\rho = 2700$ Kg/m³; $E = 69$ GPa; and $\nu = 0.3$. Models of thickness 1 mm ($t/s = 0.38\%$) and 5 mm ($t/s = 1.92\%$) were tested. The 1 mm wing was designed for high flexibility, and achieved significant out-of-plane deflections as documented in reference 18, while the 5 mm wing was rigid. The parameter λ_s , the reciprocal of the spanwise bending stiffness of the wing normalized by the free-stream dynamic pressure, was used to give an indication of the relative flexibility of the wings, whereby a higher value of λ_s corresponds to a more flexible wing. The above conditions resulted in a non-dimensional span-wise bending stiffness, $\lambda_s = 3.1$ for the 1 mm wing of all sweep angles, compared with a value of $\lambda_s = 0.025$ for the rigid wings.

Force balance measurements were undertaken using a six-component strain-gauged internal balance. Forces were normalised by qS ; moments by qSc , where q is the free-stream dynamic pressure, S is the wing reference area, and c is the root chord. Root-Mean-Square (RMS) quantities are presented following filtering of the voltage signal to remove unwanted electrical noise. Wing-tip displacements were measured using a high-speed Kodak digital camera with a resolution of 512 x 240 pixels, and a capture rate of 500 frames per second. Tip displacements were measured from the resulting images and calibrated to give measurements in SI units. Buffet response was measured by mounting Entran EGA miniature accelerometers with a mass of approximately 0.5 g on each tip of the flexible wings. Signals from the accelerometers were recorded using a desktop PC with a 12-bit A/D data acquisition card. Signals were recorded for a period of 5 s at a sampling frequency of 1000 Hz, resulting in a record spanning over 250 c/U_∞ .

Quantitative flow measurements were undertaken using PIV and LDV. For PIV, illumination of the plane of interest was achieved using a pair of pulsed mini Nd:YAG lasers with a maximum energy of 120 mJ per pulse. Images were captured using an 8-bit digital camera with a resolution of 4.2 million pixels. Each case was averaged over 100 frames at a frame rate of 3.75 Hz in order to yield a time-average spanning over 2500 c/U_∞ , and velocity vectors were calculated at over 50,000 points in each field. The flow was seeded using a commercially available theatre-smoke generator. The measurement planes for the rigid and flexible wings are shown in Figure 2(a). In practice, the distance from the wing surface was prescribed by the need to reduce surface reflections, and was in most cases around 1mm ($h/c = 0.003$). For the flexible wing, the deformation of the wing-tips interfered with this measurement plane, and so a plane offset from that on which the apex and deformed wing-tips lay was chosen.

LDV measurements were undertaken using a 300 mW air-cooled Argon-Ion laser and TSI burst correlator unit. The data rate was of the order of 200 Hz with a burst efficiency of approximately 50%, and a total of 5,000 data points were recorded for each test giving a sample period of well over 100 c/U_∞ . Measurements of the axial velocity were taken in the cross flow plane at $x/c = 0.4$ and 0.7. Single traverses vertically above the centerline were also taken at a higher resolution, and the resulting velocity profiles for the rigid and flexible wings were compared. The measurement planes and traverses are shown in Figure 2(b).

III. Results

A. Forces and Wing Deformation

Figure 4 compares the variation of lift coefficient with incidence for the flexible and rigid wings of all sweep angles tested. The results show that the lift enhancement phenomenon is not limited to wings of 50° leading edge sweep; rather, the effect of flexibility was to result in a region of enhanced lift for all wings except the 60° wing. The magnitude and extent of the lift enhancement region was a function of sweep angle, with the greatest enhancement being observed over the wing of lowest sweep. This is further demonstrated in Table 1, which lists some statistics regarding the lift curves shown in Figure 4. In this table, $\Delta C_{L_{\max}}$ represents the increment in

maximum lift coefficient achieved by the flexible wing compared with (a) C_{Lmax} of the rigid wing, and (b) C_L of the rigid wing at α_{STALL} of the flexible wing.

The 40° wing improved the maximum lift coefficient by over 40%, and at the point of stall of the flexible wing, lift coefficient was enhanced by over 50%. As sweep angle was increased the magnitude of the lift enhancement reduced, with the overall maximum lift coefficient of the 55° wing increased by just 1%, while the 60° wing experienced an overall reduction in lift. Similarly, for the 40° wing a delay in the onset of stall of 7° was achieved by the flexible wing, while no delay in stall was achieved for the 60° wing. For all the wings, the nose-down pitching moment measured about the apex underwent a similar magnitude increase in the lift enhancement region.

Λ	C_{Lmax}		ΔC_{Lmax}		$\Delta\alpha_{STALL}$
	Rigid	Flexible	(a)	(b)	
40	0.77	1.09	42%	53%	7°
45	0.83	1.14	38%	49%	6°
50	0.92	1.13	23%	45%	5°
55	1.07	1.08	1%	23%	3°
60	1.24	1.18	-5%	-5%	0

Table 1: Statistics of lift enhancement and stall delay over flexible delta wings of varying sweep angle. ΔC_{Lmax} (a) and (b) are defined in the text.

Due to the degree of flexibility employed in these experiments, considerable time-averaged and fluctuating displacements were observed. For the wings of 40°, 50° and 60° sweep, the variation of wing-tip displacement with incidence is shown in Figure 5. The data for the 50° wing was previously presented in reference 18. For the 40° and 50° wings the lift enhancement region was accompanied by an increase in both the amplitude and, to a lesser extent, mean (time-averaged) tip deflection. For the 60° wing, which did not experience an increase in lift, no such discontinuity in the displacement curves was observed. In fact, it is clear that the 60° wing experiences much less buffet than the lower sweep wings, although the peak mean deflection is greater. Although the wings were carefully designed to have identical values of λ_s , and therefore equivalent bending stiffness, the chord lengths of the wings are not equal resulting in a lower thickness-to-chord ratio for the 60° wing, and this probably accounts for the greater span-wise bending. The effect of a span-wise dihedral camber of this nature is to reduce the effective leading edge sweep angle and incidence of the wing¹⁹, and these effects are consistent with a reduction in lift. This explains why, in the absence of a lift enhancement region, the flexible 60° wing underwent a reduction in the lift-curve slope compared with the rigid wing.

Figure 6 shows the variation of RMS lift coefficient with incidence for all the wings. While there is clearly an increase in the level of buffet in the region of interest, the peak RMS lift coefficient is roughly equal for the flexible and rigid wings. This is important, as it signifies that the lift improvements can be achieved without the imposing high lift force fluctuations. The level of buffet decreases significantly with sweep angle, with peak RMS values of the 60° wing reaching just a third of that observed over the 40° wing.

Figure 7 shows the variation of RMS rolling moment coefficient with incidence for the wings. For all the wings that experienced a lift enhancement, a significant increase in RMS rolling moment was observed in the lift enhancement region for the flexible wing; this increase was not observed for the rigid wings. These data lend further evidence to suggest that the wings vibrate in an anti-symmetric mode in the lift-enhancement region. Previously, wing-tip accelerometer measurements for a 50° wing yielded signals from each side of the wing that were 180° out-of-phase¹⁸. In the current case, while significant rolling moment fluctuations have been observed in the lift-enhancement region, the fluctuations in lift force coefficient were not significantly larger for the flexible wing than for the rigid.

The question as to whether or not an anti-symmetric vibration of the wing is a necessary condition for the production of additional lift is an important one, and one that is as yet unanswered. However, further evidence may be presented to suggest that this form of vibration is indeed necessary. Figure 8 shows the variation of wing-tip RMS acceleration with incidence for a half-wing 50° flexible model, and compares this with the full wing case as presented in reference 18. Although direct measurement of the forces over the half-wing model was not possible, an increase in the level of buffet similar to that shown over the full-wing model would indicate the existence of a lift

enhancement region. However, no such increase in buffet was detected for the half-wing, suggesting that the wing did not experience an increase in lift.

The mode shapes and natural frequencies for the wings were predicted using the finite element analysis software Ansys. In all cases the mode shapes were similar to those documented for the 50° wing previously¹⁸, but the frequencies at which each mode occurred was a function of sweep angle as demonstrated in Table 2.

Λ	St					
	Mode 1	Mode 2	Mode 3	Mode 4	Mode 5	Mode 6
40	0.172 (S)	0.172 (A)	0.671 (A)	0.683 (S)	0.944 (A)	0.955 (S)
45	0.201 (S)	0.201 (A)	0.738 (A)	0.752 (S)	1.064 (A)	1.070 (S)
50	0.235 (S)	0.235 (A)	0.797 (A)	0.811 (S)	1.179 (S)	1.220 (A)
55	0.276 (S)	0.276 (A)	0.862 (A)	0.870 (S)	1.069 (S)	1.424 (A)
60	0.327 (S)	0.327 (A)	0.905 (S)	0.932 (A)	0.949 (S)	1.679 (A)

Table 2: Finite element predictions of normalised natural frequencies of test models (S – symmetric mode, A – anti-symmetric mode).

Spectral analysis of the rolling moment coefficient was undertaken, and dominant peaks were observed at frequencies approximately corresponding to the 2nd anti-symmetric modes shown in Table 2. These data are plotted in Figure 9, whence a good agreement between the finite element prediction and the experimental results can be seen; the agreement seems to improve with increasing sweep angle.

B. Flow Topology

An initial attempt to document the surface flows over 50° rigid and flexible wings was conducted previously using a fluorescent tuft technique¹⁸. It was shown for a rigid wing at $\alpha = 27^\circ$ that although a localized region of reattachment was observed near the centerline, the dominating features of the flow were its unsteady nature and the existence of significant regions of flow reversal, particularly along the leading edges. For the flexible wing, however, a much more energetic flow indicative of continued reattachment was observed. Although flow reversal was still a feature of the flow towards the leading edges, the flow was much less unsteady.

The disadvantage of the tuft visualization technique is that although an indication of flow direction may be gleaned from the video footage and still images, no indication of the velocity of the flow at any point is provided. For this purpose a more quantitative method of measurement was required. For this purpose, PIV measurements of the near-surface flow were undertaken. Figure 10 shows the magnitude of velocity near the wing surface over the rigid 50° wing at $\alpha = 27^\circ$. Note that the measurement does not encompass the entire wing surface. Figure 11 shows the streamlines calculated from the velocity vectors of the same dataset. These figures confirm that the flow over the rigid wing at this high incidence is completely stalled, with maximum velocities on the wing surface of around $u/U_\infty = 0.3$ in the flow reversal region near the leading edges. The flow towards the centerline is devoid of the high axial velocities that are associated with shear layer reattachment.

There are a number of critical points that may appear in a surface flow which, upon identification, may be used to interpret the three-dimensional flow topology. A critical point is defined as a point in the flow at which the skin friction and the velocity vector equals zero²⁰. While any point in a flow can have only a single trajectory, the existence of a singular or critical point in a flow is identified by the convergence of skin-friction lines to a single point. Examples of critical points are nodes (of separation and attachment), saddle points, and foci; all of which imply a different characteristic of the three-dimensional flow. Since this topic has been covered extensively in the literature, and a detailed discussion falls outside the remit of this paper, the reader is directed to references 20 and 21 for further reading.

A summary of the critical points identified over the rigid 50° wing is shown in Figure 12a, which indicates the existence of two saddle points (S_1 and S_2) and a node of separation (N_1) up-stream of a pair of foci (F_1 and F_2). The total number of nodes must exceed the total number of saddles on an isolated body²⁰ by 2, but clearly in the current case, since the foci are classified as nodes, there would appear to be a node missing from this interpretation. In fact, since we are considering only part of the flow this is acceptable, provided it is accepted that the resulting interpretation can only be supposition until the full surface flow pattern is documented. However, the measurements

have elucidated just enough of the surface pattern to give an indication of the separation characteristics. The fact that streamlines are directed towards a pair of foci in the manner depicted in Figure 12 suggests that flow leaves the upper surface by forming a pair of vortices, as shown in the three-dimensional interpretive sketch that forms Figure 12a. The remainder of the flow is directed upstream, and the source of this is likely to be flow ‘leaking’ over the trailing edge. At some point, due to the pressure gradient, this flow forms the pair of vortices that curve up into the free stream, while the remaining surface flow continues towards the apex, where it will separate in proximity with the separated shear layer.

Figure 13 shows the magnitude of the near surface time-averaged velocity over the flexible wing at $\alpha = 27^\circ$, while Figure 14 shows the streamlines calculated from the velocity vector field. Contrary to the streamlines over the rigid wing, the flexible wing demonstrates a symmetrical time-averaged flow. Significant regions of flow reversal are observed over the wing, with high negative axial velocities peaking at $u/U_\infty = -0.38$. Along the centerline, high positive axial velocities are observed, peaking at around $u/U_\infty = 0.67$. A node exists on the centerline at around $x/c = 0.2$, and all surface streamlines on the wing issue from this node, indicating that it is a node of attachment. A pair of saddle lines exist that separate the flow into that which, having attached to the wing surface, continues with high velocity directly downstream, and that which becomes entrained into the region of tip stall and flow reversal along the leading edges. Figure 15a shows the locations of the identified critical points, on which the saddle lines are shown as (S_1) and (S_2) . Figure 15b shows the three-dimensional interpretation of the time-averaged flow. This interpretation has the shear layer, which separates from the leading edges, reattaching inboard of the leading edges on the suction surface, and curling up to result in flow reversal in this region. Flow that is not entrained into the tip-stall region, passes over the detached shear layer, and reattaches aft of the attachment node to result in the high axial velocities observed along the centerline.

Similar streamline patterns have also been observed over rigid wings of 38.7° leading edge sweep²² at $\alpha = 10^\circ$, and of 50° sweep¹¹ at $\alpha = 20^\circ$. The similarity between the surface flow topologies between these two cases is very good, despite the very different flow conditions. However, in neither case was an attachment node recorded along the centerline, indicating that the flow around the apex does not separate and remains attached along the length of the wing. This is likely to be due to the lower incidences of these wings compared with the flexible wing being studied herein.

The data therefore show that the flow over the flexible wing is much more coherent than that over the rigid wing at the same incidence. The flexibility clearly results in fundamental improvements to the flow, and allows the shear layer to continue to reattach to much higher angles of attack than would otherwise be expected.

Off-surface flows were also documented in the course of this research. Figure 16 shows the results of a LDV measurements of the chordwise velocity field in the cross-flow plane at $x/c = 0.7$ for the (a) rigid and (b) flexible 50° wings at $\alpha = 25^\circ$. For the rigid wing, the flow is much more symmetric and coherent than suggested by the PIV measurements presented above for $\alpha = 27^\circ$. The data show a large region of reversed flow extending well above the surface of the wing, but a region of high axial velocity remains along the centre-line, albeit at a considerable distance from the wing surface. Comparing Figure 16 with Figure 11 indicates that the difference of 2° of incidence between the two measurements was significant. At $\alpha = 25^\circ$, the LDV measurements indicate that the flow over the rigid wing is still semi-attached, while at 27° the PIV measurements suggest the opposite to be true.

The chordwise velocity field over the flexible wing shares many similarities with that of the rigid wing. Again, a region of reversed flow extending well above the wing surface is evident along with a region of high axial velocity above the surface near the centre-line. However, the region of flow reversal is reduced in extent and appears flatter than for the rigid wing, while the region of high axial velocity above the centre-line is larger and extends closer to the wing surface.

Figure 17 shows the axial velocity profiles measured above the centre-line of the rigid and flexible 50° wings at (a) $x/c = 0.4$ and (b) $x/c = 0.7$. For both cases, the flexible wings exhibit much higher axial velocities towards the wing surface than do the rigid wings, while further away from the wing the velocity profiles merge.

IV. Conclusions

Force measurements have demonstrated the ability of a flexible non-slender delta wing to enhance lift and delay stall compared with a rigid wing of similar geometry. The work has extended the results of a recent study to include data for a range of wings with varying sweep angle. Over the range of sweep angles tested the greatest lift enhancement was observed over the wing with smallest leading edge sweep, while for the only slender wing considered no lift enhancement was observed. This indicates that it is a feature of the fundamentally different flow that occurs over low-sweep wings that is responsible for the phenomenon.

Significantly, the variation of RMS lift force with incidence for the rigid and flexible cases shows good comparison, while the RMS rolling moment coefficients for the flexible wings were much higher than the rigid wings in the lift enhancement region. This indicates that the wings are vibrating in an anti-symmetric structural mode, and confirms the results of a previous investigation. To further investigate the role of this anti-symmetric vibration in the lift enhancement phenomenon, RMS wing-tip acceleration measurements for a full and half-wing 50° model were compared. These results indicated that the half-wing model did not experience an increase in lift, and may suggest that the anti-symmetric vibration is therefore a necessary condition for the lift enhancement to occur.

PIV and LDV measurements have demonstrated the striking difference between the flows over the flexible and rigid wings in the post-stall region at $\alpha = 25^\circ$ and 27° . The effect of flexibility is to reduce the extent to the region of flow reversal that occurs over the wing surface, and to promote the reattachment of the shear layer to higher incidences.

Acknowledgments

This material is based upon work supported by the European Office of Aerospace Research and Development, Air Force Office of Scientific Research, Air Force Research Laboratory, under Contract No. F61775-02-C4024.

References

1. Earnshaw, P. B. and Lawford, J. A., "Low-Speed Wind-Tunnel Experiments on a Series of Sharp-Edged Delta Wings", ARC Reports and Memoranda No. 3424, March 1964.
2. Wéntz, W. H. and Kohlman, D. L., "Vortex Breakdown on Slender Sharp-Edged Wings", *Journal of Aircraft*, vol. 8, no. 3, March 1971, pp. 156-161.
3. Lee, M. and Ho, C., 'Lift force of delta wings', *Applied Mechanics Review*, Vol. 43, No. 9, pp. 209-221, 1990.
4. Mueller, T. J. and DeLaurier, J. D., "Aerodynamics of Small Vehicles", *Annual Review of Fluid Mechanics*, Vol. 35, pp. 89-111, 2003.
5. Gordnier, R. E. and Visbal, M. R., "Higher-Order Compact Difference Scheme Applied to the Simulation of a Low Sweep Delta Wing Flow", AIAA 2003-0620, 41st AIAA Aerospace Sciences Meeting and Exhibit, 6-9 January 2003, Reno, NV.
6. Taylor, G. S., Schnorbus, T., and Gursul, I., "An Investigation of Vortex Flows over Low Sweep Delta Wings", AIAA-2003-4021, 33rd AIAA Fluid Dynamics Conference, 23-26 June, Orlando, FL.
7. Moore, D. W. and Pullin, D. I., "Inviscid Separated Flow over a Non-slender Delta Wing", *Journal of Fluid Mechanics*, vol. 305, 1995, pp. 307-345.
8. Gursul, I., Taylor, G., and Wooding, C., "Vortex Flows over Fixed-Wing Micro Air Vehicles", AIAA 2002-0698, 40th AIAA Aerospace Sciences Meeting & Exhibit, 14-17 January 2002, Reno, NV.
9. Erickson, G. E., "Water Tunnel Studies of Leading Edge Vortices", *Journal of Aircraft*, Vol. 19, No. 6, pp. 442-448, 1982.
10. Ol, M. V. and Gharib, M., "Leading-Edge Vortex Structure of Nonslender Delta Wings at Low Reynolds Number", *AIAA Journal*, Vol. 41, No. 1, January 2003, pp. 16-26.
11. Taylor, G. S. and Gursul, I., "Unsteady Vortex Flows and Buffeting of a Low Sweep Delta Wing", AIAA-2004-1066, 42nd AIAA Aerospace Sciences Meeting & Exhibit, 5-9 January 2004, Reno, NV.
12. Gray, J., Gursul, I. and Butler, R., 2003, "Aeroelastic Response of a Flexible Delta Wing Due to Unsteady Vortex Flows", AIAA-2003-1106, 41st Aerospace Sciences Meeting and Exhibit, 6-9 January, Reno, NV.
13. Gordnier, R. and Visbal, M. R., 'Computation of the Aeroelastic Response of a Flexible Delta Wing at High Angles of Attack', AIAA-2003-1728.
14. Menke, M., Yang, H., and Gursul, I., 'Experiments on the unsteady nature of vortex breakdown over delta wings', *Experiments in Fluids*, Vol. 27, pp. 262-272, 1999.
15. Gursul, I., "Unsteady Flow Phenomena over Delta Wings at High Angle-of-Attack", *AIAA Journal*, Vol. 32, No. 2, 1994, pp. 225-231.
16. Maybe, D. G., "Beyond the Buffet Boundary", *Aeronautical Journal*, Vol. 77, April 1973, pp. 201-205.
17. Gursul, I., "Recent Developments in Delta Wing Aerodynamics", *Aeronautical Journal*, September 2004, pp. 437-452..
18. Taylor, G. S. and Gursul I., 'Lift Enhancement over a Flexible Low Sweep Delta Wing, AIAA-2004-2618 2nd AIAA Flow Control Conference, 27 June – 1 July 2004, Portland, OR.
19. Traub, L. W., "Lift Prediction of Spanwise Cambered Delta Wings", *Journal of Aircraft*, Vol. 36, No. 3, pp. 515-522, May-June 1999.
20. Détery, J. M., "Physics of Vortical Flows", *J. Aircraft*, Vol.29. No. 5, pp. 856-876, 1992.
21. Détery, J. M., "Robert Legendre and Henry Werle: Towards the Elucidation of Three Dimensional Separation", *Annual Review of Fluid Mechanics*, Vol. 33, pp. 129-154, 2001.
22. Yavuz, M. M., Elkhoury, M., and Rockwell, D., "Near-Surface Topology and Flow Structure on a Delta Wing", *AIAA Journal*, Vol. 42, No. 2, pp. 332-340, 2004.

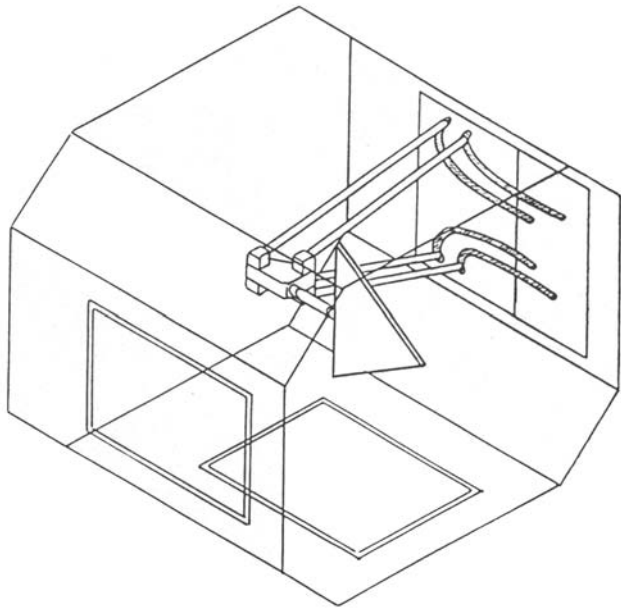


Figure 1: Schematic of the working section and high incidence mechanism, 7' x 5' wind tunnel.

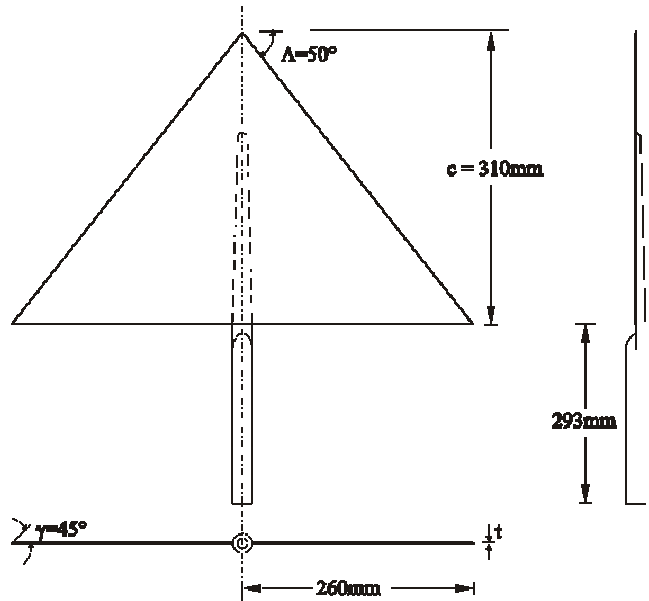
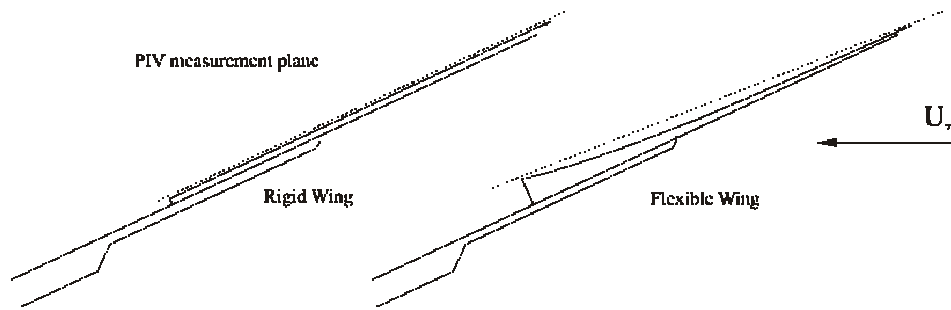
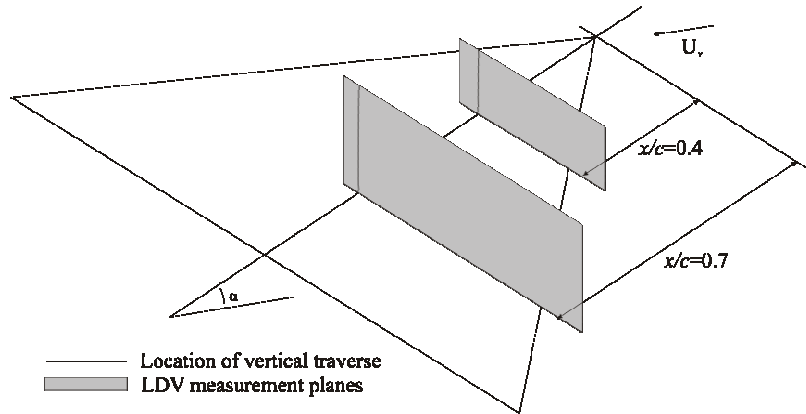


Figure 3: Principle model dimensions of flexible wing with leading edge sweep, $\Delta = 50^\circ$.



(a) Locations of PIV measurement planes.



(b) Locations of LDV measurement planes.

Figure 2: PIV and LDV measurement planes

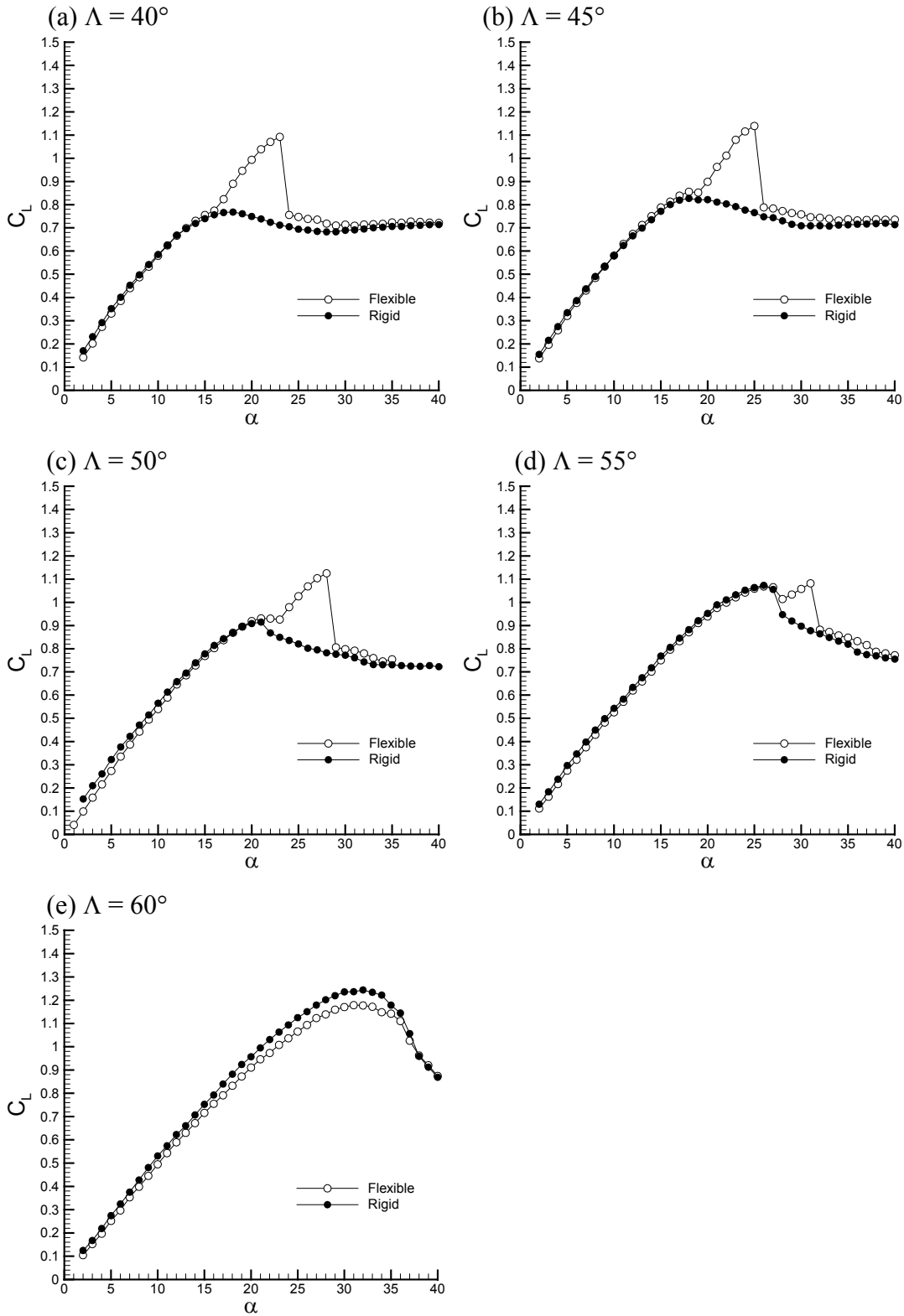
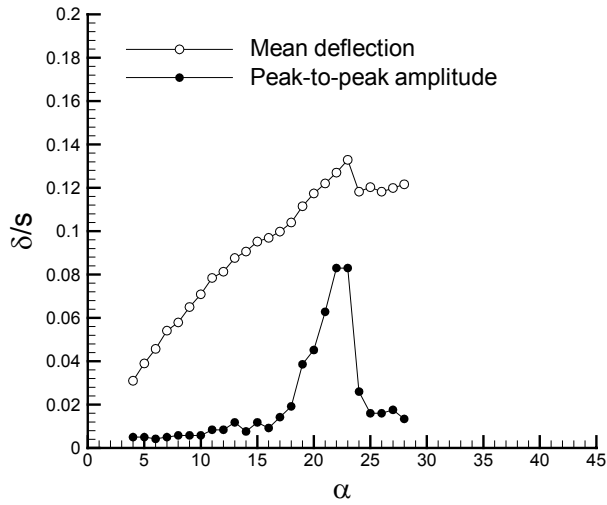
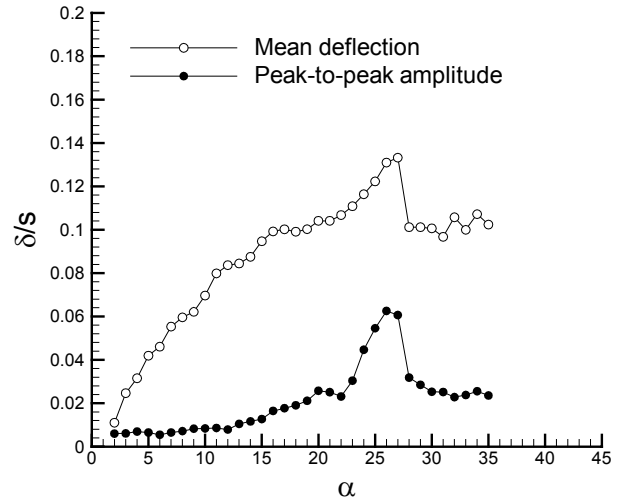


Figure 4: Variation of magnitude of lift coefficient with incidence for all wing tested.

(a) $\Lambda = 40^\circ$



(b) $\Lambda = 50^\circ$



(c) $\Lambda = 60^\circ$

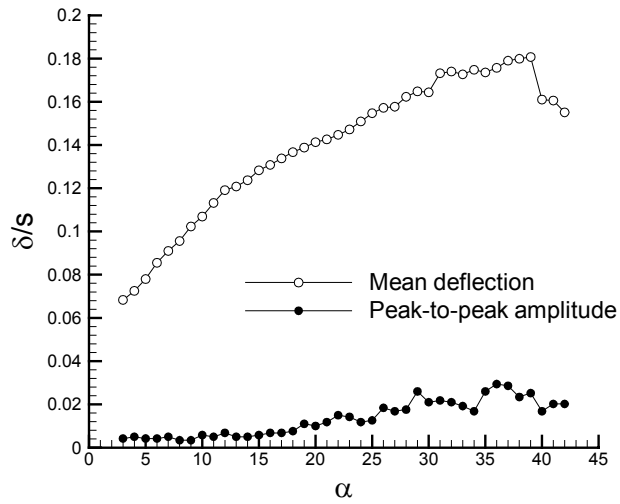


Figure 5: Variation of time-averaged and fluctuation amplitude of wing-tip deflections with incidence.

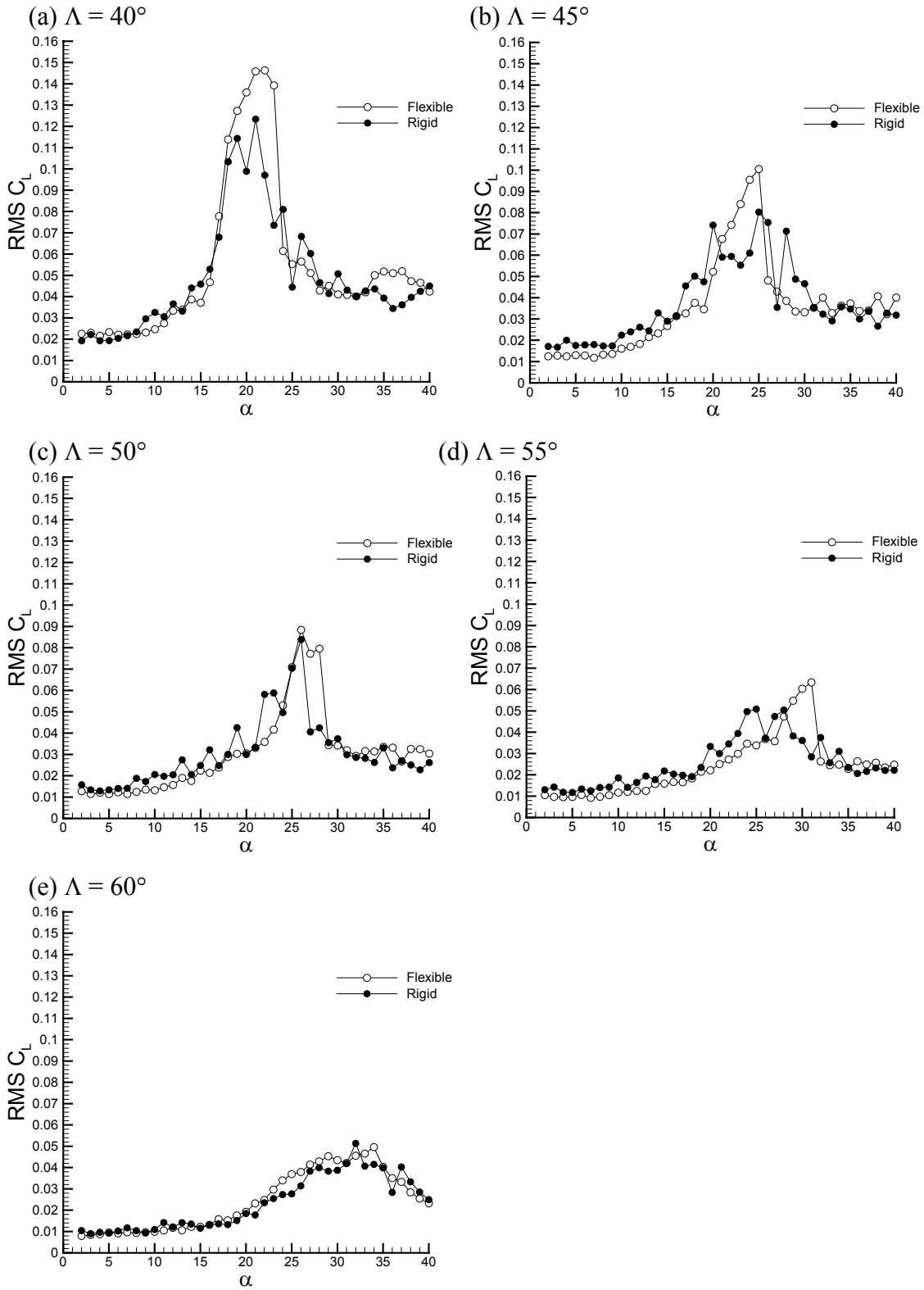


Figure 6: Variation of RMS lift coefficient with incidence.

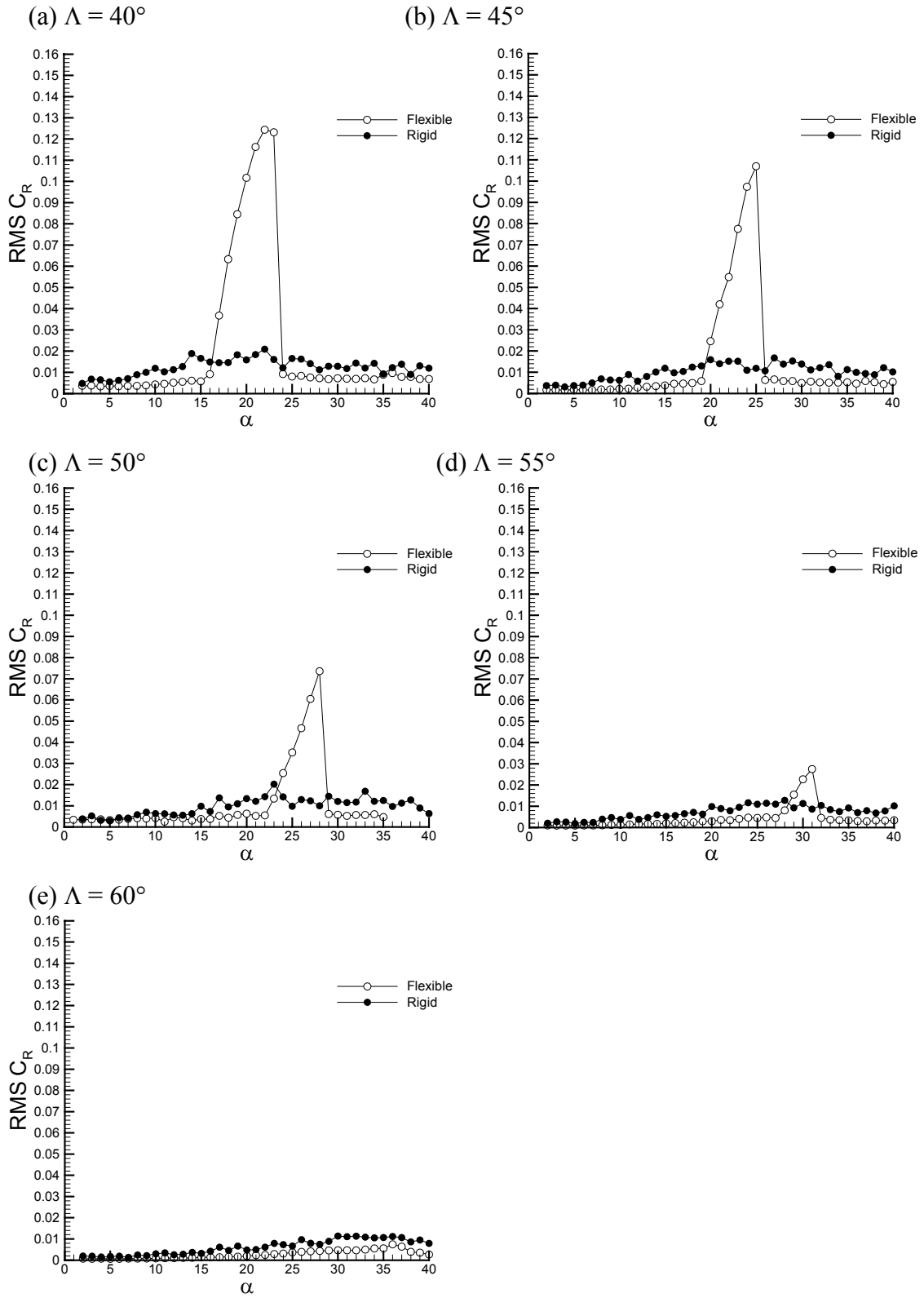


Figure 7: Variation of RMS rolling moment coefficient with incidence.

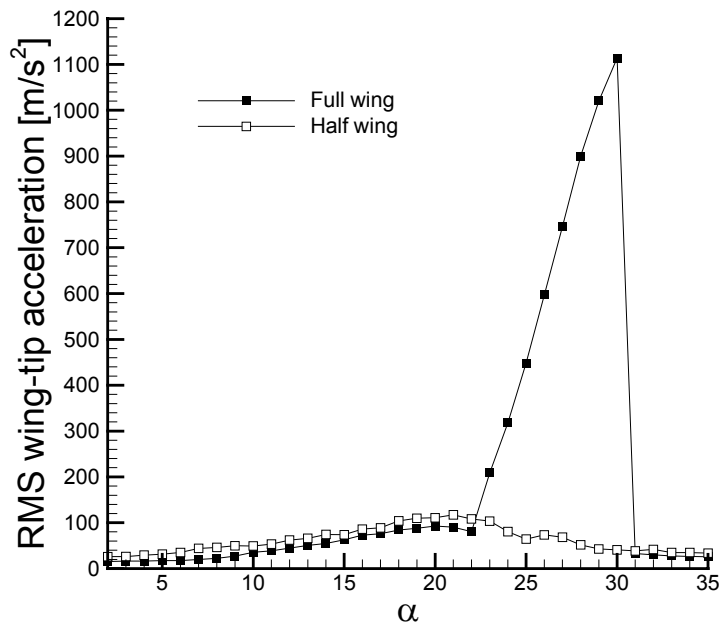


Figure 8: Variation of RMS wing-tip acceleration for 50° half-wing model, compared with that of full wing model from reference 18.

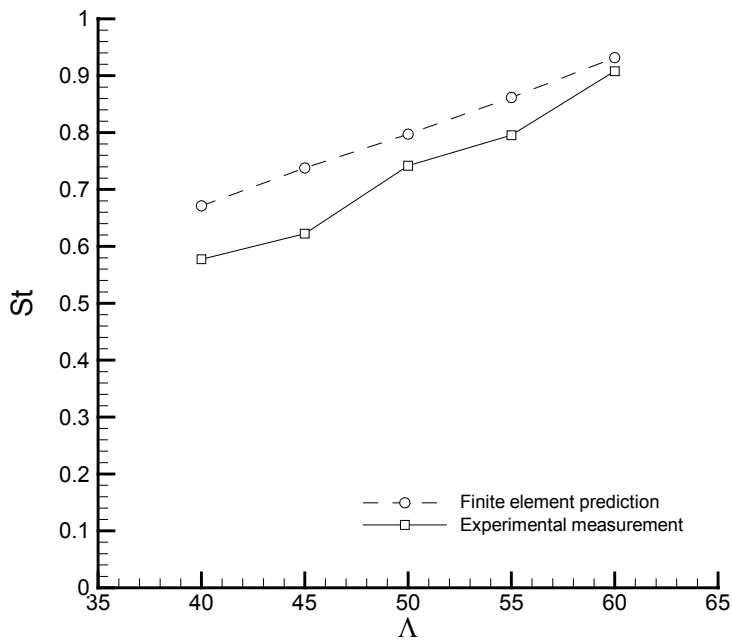


Figure 9: Comparison of frequency of second anti-symmetric mode predicted by finite element models with dominant frequencies in rolling moment spectra.

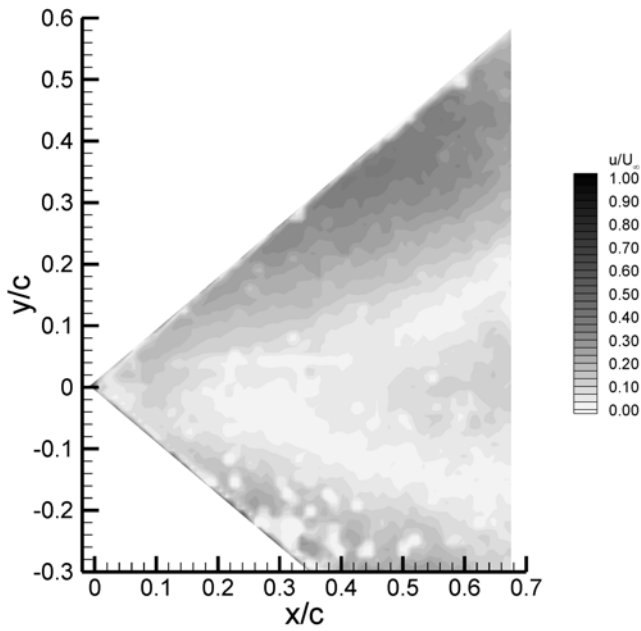


Figure 10: Near surface time-averaged velocity field at $\alpha = 27^\circ$, rigid wing, $\Lambda = 50^\circ$.

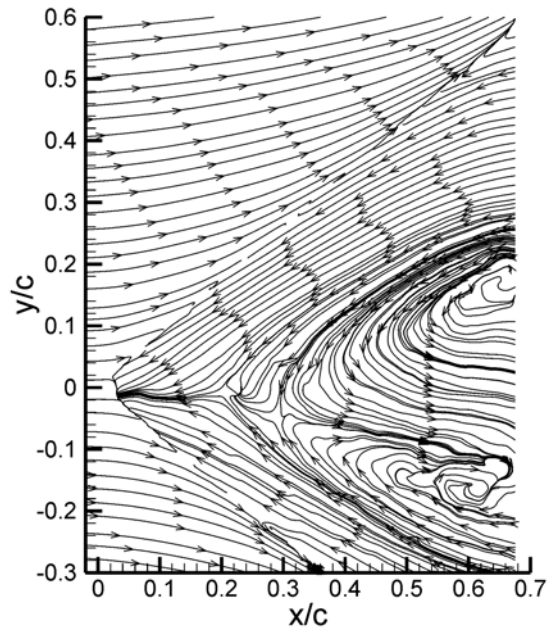


Figure 11: Near surface time-averaged streamlines at $\alpha = 27^\circ$, rigid wing, $\Lambda = 50^\circ$.

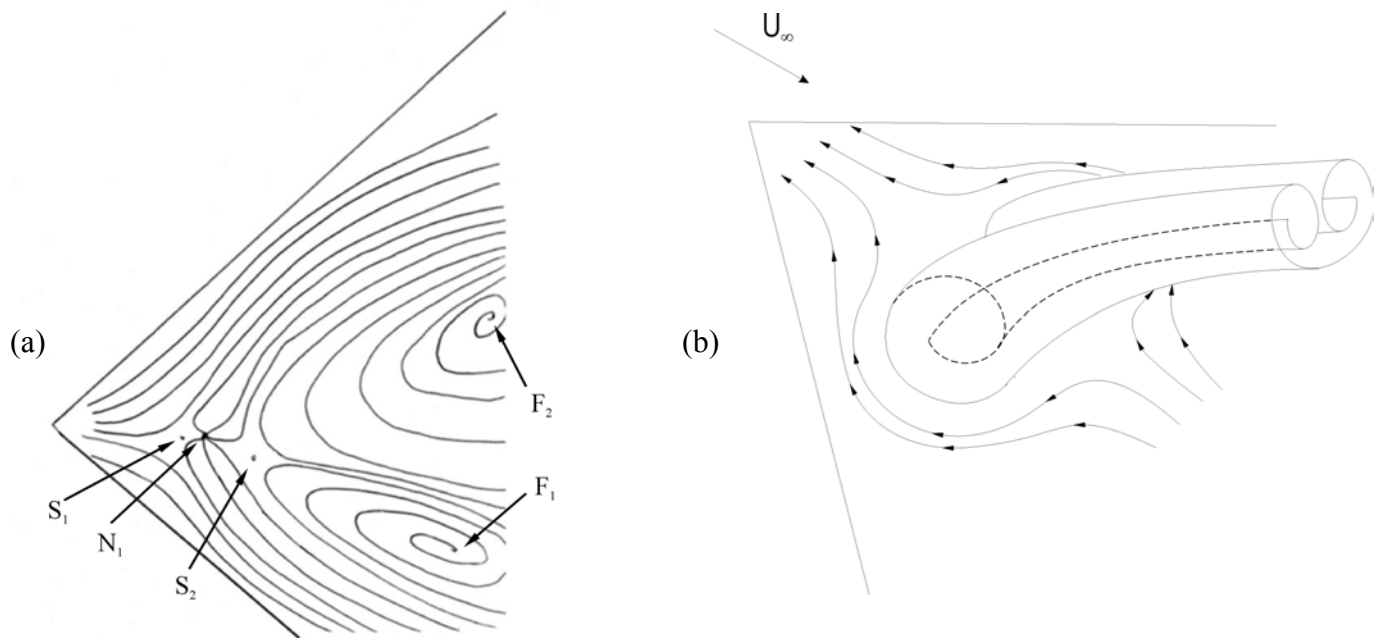


Figure 12: (a) 2D and (b) 3D topological interpretations of the near-surface flow over the rigid 50° wing at $\alpha = 27^\circ$.

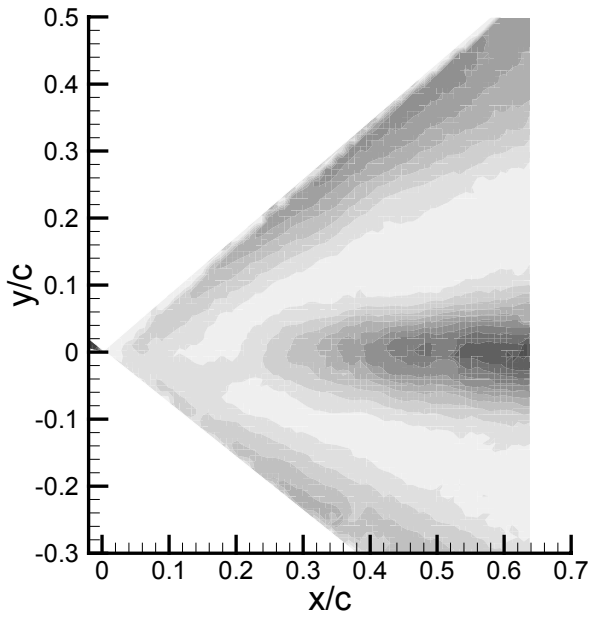


Figure 13: Near surface time-averaged velocity field at $\alpha = 27^\circ$, flexible wing, $\Lambda = 50^\circ$.

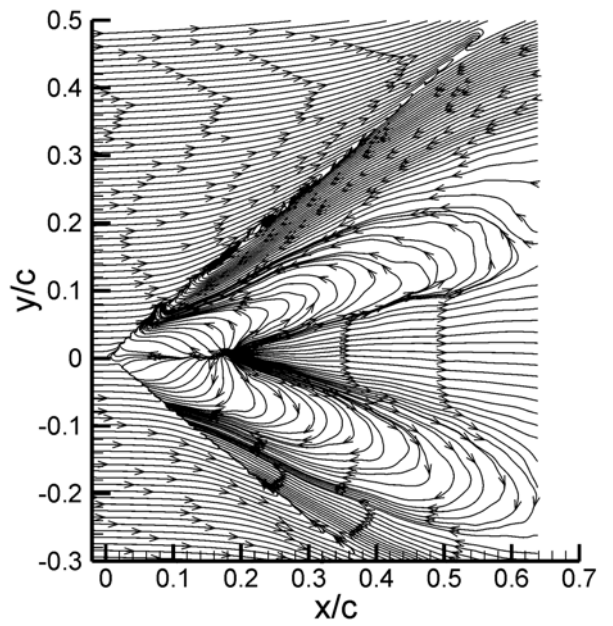


Figure 14: Near surface time-averaged streamlines at $\alpha = 27^\circ$, flexible wing, $\Lambda = 50^\circ$.

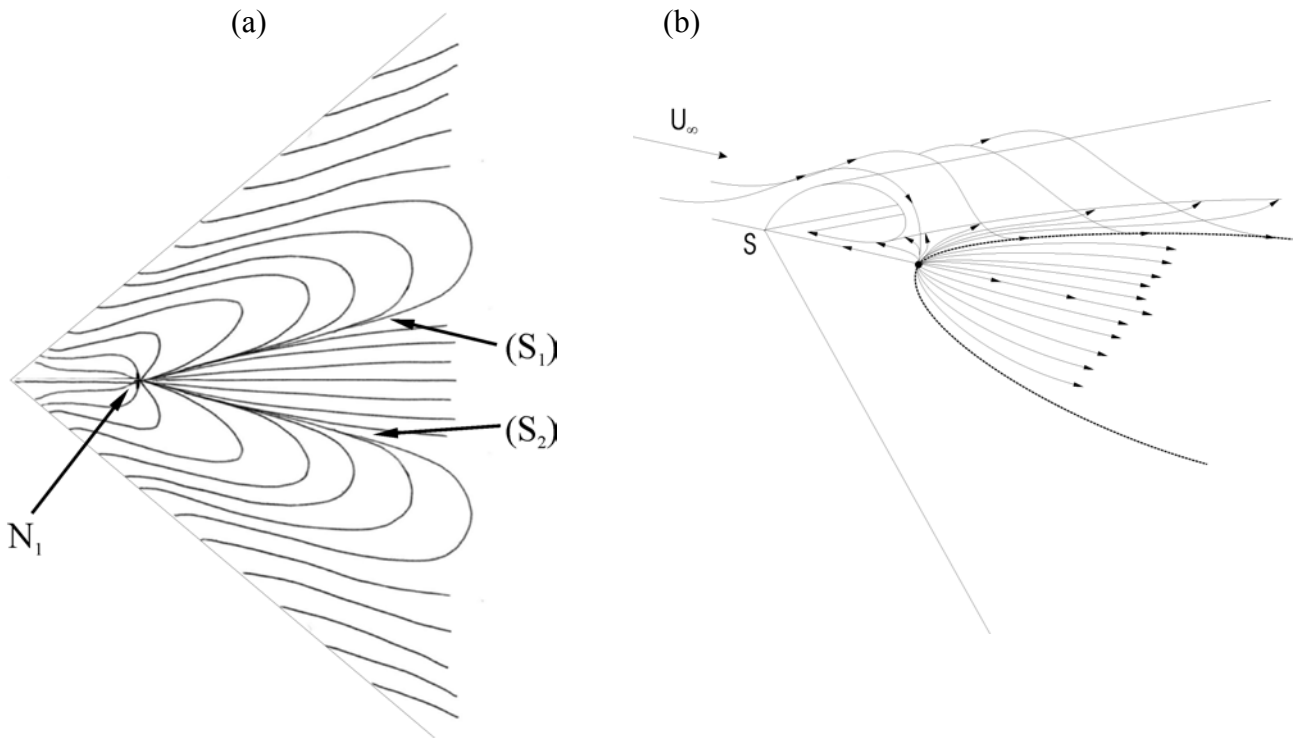


Figure 15: (a) 2D and (b) 3D topological interpretations of the near surface flow over the flexible 50° wing at $\alpha = 27^\circ$.

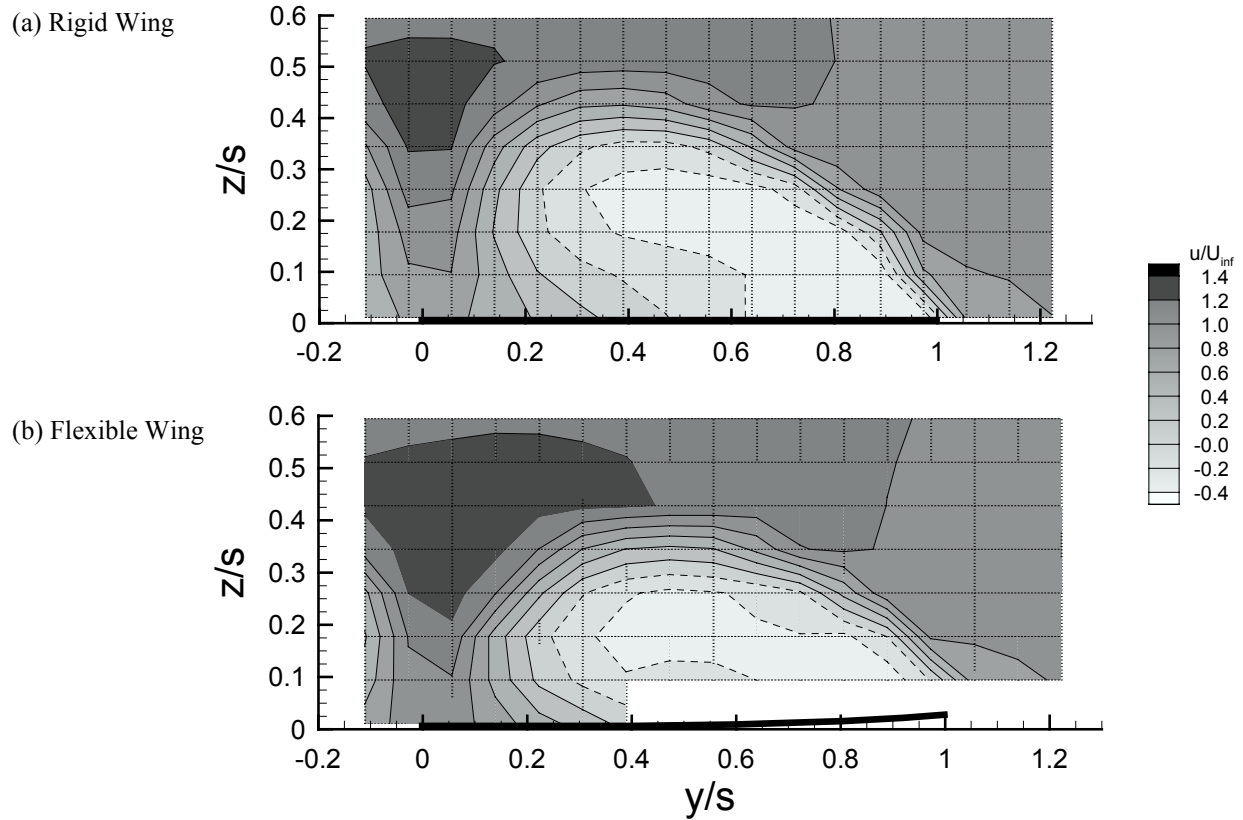


Figure 16: Comparison of axial velocity fields measured in the cross-flow plane at $x/c = 70\%$, $\Lambda = 50^\circ$ wing at $\alpha = 25^\circ$. Intersection of grid lines corresponds to measurement point.

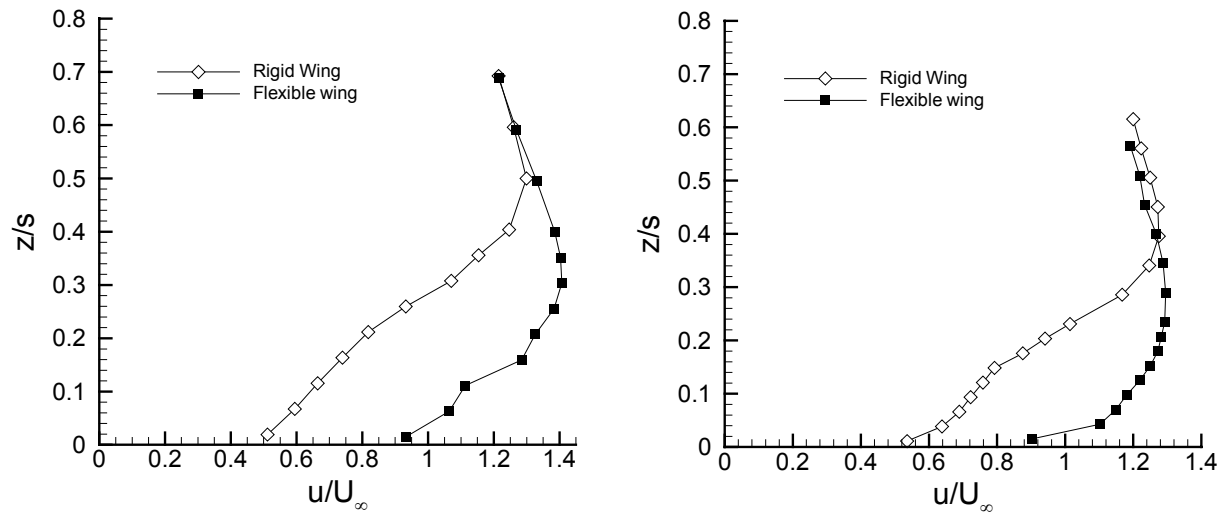


Figure 17: Axial velocity profile above wing centre-line at (left) $x/c = 0.4$ and (right) $x/c = 0.7$ ($\Lambda = 50^\circ$ wing at $\alpha = 25^\circ$).

Physical Mechanisms of Lift Enhancement for Flexible Delta Wings

E. Vardaki^{*}, I. Gursul[†] and G. S. Taylor[‡]
University of Bath, Bath BA2 7AY, United Kingdom

Passive lift enhancement for flexible nonslender delta wings has been demonstrated as a potential method for the control of vortex-dominated wing flows. Physical mechanisms of lift enhancement and the effect of important variables are discussed. Lift enhancement for flexible wings with low/moderate sweep is a very complex phenomenon, involving self-induced antisymmetric vibrations of leading edges, spanwise camber effect due to the large time-averaged deflection, shear layer instabilities, reattachment, increased mean vorticity flux and circulation, re-formation of the leading edge vortices, possible enhancement of streamwise pressure gradient, and the effects of frequency and edge velocity.

Nomenclature

c	=	chord length
f	=	frequency
fc/U_∞	=	dimensionless frequency
s	=	semi-span
t	=	wing thickness
q	=	free-stream dynamic pressure
C_L	=	coefficient of lift
E	=	elastic modulus
Re_c	=	chord Reynolds number
S	=	wing reference area
U_∞	=	free-stream velocity
α	=	angle of attack
λ_s	=	spanwise bending stiffness normalized by free-stream dynamic pressure ($= 12(1-\nu^2)\rho_\infty U_\infty^2 s^3/Et^3$)
ν	=	Poisson's ratio
ρ	=	density
Λ	=	leading-edge sweep angle

I. Introduction

PASSIVE lift enhancement for flexible delta wings has been demonstrated as a potential method for the control of vortex-dominated wing flows^{1,2}. Force measurements over a range of non-slender delta wings (with sweep angles $\Lambda = 40^\circ$ to 55°) have demonstrated the ability of a flexible wing to enhance lift and delay stall compared with a rigid wing of similar geometry. An example for $\Lambda = 50^\circ$ is shown in Figure 1. It is seen that lift enhancement was achieved in the post-stall region. Both an increase in time-averaged lift coefficient of up to 45%, and a delay in stall of up to 9 degrees were observed. For the only slender wing considered, of 60° leading edge sweep, no lift enhancement was observed, indicating that it is a feature of the fundamentally different flow that occurs over low sweep wings that is responsible for the phenomenon. The main objective of this paper is to review the physical mechanisms of lift enhancement and to discuss the most important variables for flexible nonslender delta wings.

^{*} Postgraduate Student, Department of Mechanical Engineering, Student Member AIAA.

[†] Professor, Department of Mechanical Engineering, Associate Fellow AIAA.

[‡] Post-Doctoral Research Associate, Department of Mechanical Engineering, Member AIAA.

II. Experimental methods

Wind tunnel experiments were conducted in the high speed working section of the 7 x 5 foot closed circuit facility at the University of Bath. Models were supported using the high-incidence rig as shown in Figure 2, and various leading edge sweep angles and thickness were tested. Each model was a planar delta wing with a pressure surface leading edge bevel of 45° , and a square trailing edge. Experiments were conducted at a constant free stream velocity of $U_\infty = 31$ m/s, resulting in chord Reynolds numbers in the range 440,000 – 900,000. Each model was made from aluminium alloy 1050A, which has the following material properties: $\rho = 2700$ Kg/m³; $E = 69$ GPa; and $\nu = 0.3$. Maximum blockage for the wind tunnel was approximately 2.3% for the 60° wing at $\alpha = 50^\circ$. Force balance measurements were undertaken using a six-component, strain-gauged internal balance. Forces are normalised by qS . Surface flow visualizations were achieved using lengths of thin fluorescent thread taped to the wing. Quantitative flow measurements were undertaken using Digital Particle Image Velocimetry (DPIV). Illumination of the plane of interest was achieved using a pair of pulsed mini Nd:YAG lasers with a maximum energy of 120 mJ per pulse. Images were captured using an 8-bit digital camera with a resolution of 4.2 million pixels.

In addition to the extensive wind tunnel experiments, complementary experiments were conducted in a water tunnel facility located at the University of Bath. The tunnel is an Eidetics Model 1520 free surface water tunnel, which has a 0.381 m x 0.508 m x 1.524 m test section and can achieve speeds up to 0.45 m/s through a closed circuit continuous flow system. The tunnel has four viewing windows, three surrounding the working section and one downstream allowing axial viewing. The height of the test section above the floor is adequate to allow flow visualisation viewing from below as well as from the sides. The tunnel also incorporates dye system with six available dye tubes to enable flow visualization with different colours.

Experiments were conducted using an aluminium low sweep angle delta wing model with 50° sweep angle. The model had a 45° bevel on the leading and trailing edges on the pressure surface. The bevelling of the model was done in order to produce a sharp leading edge, which ensured the proper formation of the leading edge vortices. The model had a chord length of $c = 89$ mm and a thickness of $t = 2$ mm, giving a thickness to chord ratio, $t/c = 2.25\%$. It was mounted upside down on the tunnel using a sting projecting from the rear of the model, as shown in Figure 2. Additionally, experiments on 50° sweep angle delta wings with various flexibilities were carried out. Four different flexible wings were tested with thickness of 0.1905 mm, 0.254 mm, 0.381 mm and 0.508 mm respectively. The former two wings were made out of polyester and the latter two out of polypropylene.

Visualisation of the vortex trajectories was achieved using food colouring dye, diluted 1:4 with water. A digital video camera, with a capture rate of 25 frames per second and a resolution of 570,000 pixels, was used to capture images from the dye flow visualisation, and was interfaced to a desktop computer via the commercial software package Pinnacle Studio DV, enabling real time viewing of the wing and the capture of camera images and video recordings. The measurement uncertainty in locating the vortex breakdown position was approximately 2% of the chord length.

For PIV measurements, the flow was seeded with commercially available hollow glass particles of mean diameter of 4 μ m and the PIV camera was placed near the downstream viewing window, as shown in Figure 3. To illuminate the desired planes, the laser system was placed underneath the test section of the water tunnel, as shown in Figure 3. A combination of cylindrical and spherical lenses was used to generate the required light sheet. Images were captured using an 8-bit digital camera with a resolution of 2048 x 2048 pixels and a maximum capture rate of 7.5 frames per second, producing 3.75 frames in cross-correlation. The commercial software package Insight v6.0 and a Hart cross-correlation algorithm were used to analyse the images, with an interrogation window size of 32 by 32 pixels, and to produce velocity vectors for further processing. Sequences of 30 instantaneous frames were taken for each case and the time-averaged (or phase-averaged for dynamic roll motion) velocity and vorticity fields were calculated. PIV images for the delta wing were captured at 80% of the chord length and at a zero roll angle for both the dynamic and static cases. For the dynamic case, the PIV system was triggered in order to capture the flow field at zero roll angle and then perform phase averaging. The Reynolds number, based on the chord length, was $Re_c = 26,000$ for all the experiments.

III. Results

A. Antisymmetric vibrations

Vibrations in the second anti-symmetric mode (see Figure 4a) accompany lift enhancement. Figure 4b shows the variation of root-mean-square of wing tip acceleration as a function of incidence. It is seen that there is a sudden increase of tip acceleration in the region corresponding to lift enhancement. These large amplitude vibrations occur as a result of flow/structure interaction. The existence of self-induced antisymmetric vibrations in this region is similar to the vortex interactions discussed in a recent review article³. The details of this spectacular flow/structure interaction remain to be studied. Also, one of the remaining unresolved issues is the role of the antisymmetric vibrations and whether they are essential for lift enhancement. Recent evidence² indicates that antisymmetric interactions are essential as a half-model delta wing did not exhibit self-excited vibrations and lift enhancement.

B. Spanwise camber

Large time-averaged structural deflections also exist, which produce spanwise camber. Although there are significant time-averaged deflections of the wing, particularly at high incidences, these are unlikely to contribute to the lift enhancement phenomenon¹. Figure 5 shows the variation of lift coefficient with incidence for the flexible wing and a rigid curved wing, which has the approximate shape of the time-averaged deflection of the flexible wing. It is seen that the curved wing does not exhibit similar lift enhancement.

Note that no streamwise vortex is expected, even for the flexible wing in the lift-enhancement region, as the leading edge vortices already break down at the apex for these incidences. However, a study of the effect of dihedral applied to highly swept delta wings showed an overall decrease in lift coefficient⁴. Figures 3 and 5 suggest that this effect is negligible for the nonslender wing at low incidences when leading edge vortices exist. Lift force prior to stall is unchanged, while it is only in the post-stall region that the lift enhancement is observed.

C. Reynolds number effect

In general, the Reynolds number effect is more pronounced for nonslender wings⁵, as the vortical structures form closer to the wing surface and strong interactions with wing boundary layer take place. However, even for a nonslender wing with sweep angle $\Lambda = 50^\circ$, the flow approaches an asymptotic state at higher Reynolds numbers (around 30,000), with further increases in the Reynolds number resulting in only small variations in the location of vortex core and breakdown.

A comparison of time-averaged velocity in a plane through the vortex core in water tunnel experiments ($Re = 26,000$) and in wind tunnel experiments ($Re = 620,000$) is given in Figure 6. It is seen that the time-averaged breakdown location is nearly the same, although there are some differences in the core structure and near the wing centreline. Furthermore, since the lift enhancement is observed in the post-stall region for the rigid wing, Reynolds number effect is expected to be negligible.

D. Shear layer reattachment

Surface tuft visualization and PIV measurements near the wing surface for the rigid wing show that the flow is fully separated in the post-stall regime^{1,2}. However, for the flexible wing, shear layer reattachment is observed, extending the region of partially attached flow at high incidences. The main mechanism for lift enhancement seems to be related to the excitation of the shear layer instabilities. For $\Lambda = 50^\circ$ wing, the dominant frequency of structural vibration was around $St = 0.75$, which compares well with the dominant frequencies of the shear layer instabilities^{6,7}. The self-induced vibrations of the wing energize the vortices shed into the shear layer and promote reattachment to the wing surface, resulting in delayed stall and increased lift. This is similar to the response of the flow over a backward-facing step to the periodic excitation. It is well known that, for both laminar and turbulent separation⁸, excitation enhances the formation of vortical structures and substantially reduces reattachment length.

Flow visualizations for a rigid and various flexible wings are shown in Figure 7 for $\alpha = 20^\circ$ and $\Lambda = 50^\circ$. Here, the parameter λ_s is the spanwise bending stiffness normalized by free-stream dynamic pressure, i.e., $\lambda_s = 12(1-\nu^2)\rho_\infty U_\infty^2 s^3/Et^3$, where E is elastic modulus, ν Poisson's ratio, s semi-span, and t thickness of the wing. The dye-free region near the wing centreline is much broader for the flexible wings, indicating earlier reattachment of the separated flow. For the most flexible wing ($\lambda_s = 21.28$), it is

interesting that re-formation of the leading edge vortex and rapid breakdown are visible in a region very close to the wing apex. This will be discussed in detail later on in the paper.

Figure 8 shows the vectors and contours of magnitude of time-averaged velocity in a crossflow plane at $x/c = 0.80$ for rigid and flexible wings for an even larger incidence of $\alpha = 25^\circ$. For the rigid wing, there is no reattachment, however, for the flexible wings, there is larger velocity near the wing centerline and reattachment in the time-averaged sense.

E. Mean vorticity flux

For the rigid and flexible wings, the vorticity distributions in a crossflow plane at $x/c = 0.80$ based on PIV measurements are shown in Figure 9 for $\alpha = 20^\circ$. There are substantial effects on the vortical flow with increasing wing flexibility, as the oscillating leading edge is an unsteady source of vorticity. In fact, the time-averaged vorticity flux is expected to increase with the vibrations of the leading-edge, as this term is proportional to $\overline{U_s^2}$, where U_s denotes the velocity outside the boundary layer at the separation point. This is confirmed by the larger values of vorticity for the flexible wings in Figure 9. The variation of circulation with the spanwise bending stiffness normalized by free-stream dynamic pressure, λ_{s_3} , is shown in Figure 10. It is seen that the circulation of the vortical flow in a crossflow plane increases with flexibility in comparison to the rigid wing.

F. Vortex re-formation

In order to simulate the effect of antisymmetric vibrations, experiments with a rigid wing undergoing small amplitude rolling motion were also conducted. This approach has the advantage of independent control of the frequency parameter, which cannot be varied for a flexible wing without affecting the amplitude of vibrations. Figure 11 shows flow visualization for the stationary and rolling delta wing (with an amplitude of 5°) for an incidence of $\alpha = 25^\circ$. It is seen that the totally separated flow for the stationary wing becomes very organized for the rolling wing with increasing frequency. The most interesting observation is the re-formation of the leading edge vortices at high frequencies. Although the leading edge vortices become stronger due to the leading edge motion, vortex breakdown is delayed for the rolling wing compared to the stationary wing for which breakdown is at the apex. This appears to be in contrast to the well-known studies of vortex breakdown, which indicate that increased strength of vortices should cause premature, rather than delayed, breakdown. This result suggests that streamwise pressure gradient might be modified favorably due to the wing motion.

G. Optimum frequency

Figure 12 shows the variation of mean breakdown location as a function of dimensionless frequency for different angles of attack in the range $\alpha = 20^\circ$ to 30° . It is seen that, for each incidence in the post-stall region, the breakdown location is zero for the stationary wing ($fc/U_\infty = 0$). Maximum delay of the vortex breakdown location is achieved in the range of $fc/U_\infty = 1$ to 2. Again, this range compares well with the dominant frequencies of the shear layer instabilities^{6,7} for a nonslender wing of $\Lambda = 50^\circ$.

Figure 13 compares the variation of mean breakdown location as a function of dimensionless frequency for two amplitudes of rolling motion for $\alpha = 25^\circ$. Even for the small amplitude of 1° , it is possible to have re-established leading edge vortices. The optimum dimensionless frequency is also in the same range.

H. Leading edge velocity

In the case of the rigid wing undergoing small amplitude rolling motion, the dimensionless frequency fc/U_∞ is not only a ratio of time scales of convective time and rolling motion, but also the ratio of the leading edge velocity and freestream velocity for a given wing. Figures 12 and 13 suggest that increasing velocity of leading edge (with increasing frequency parameter) does not necessarily delay breakdown location. However, it is expected that the time-averaged vorticity flux will increase with increasing velocity of the leading edge. This is confirmed by the vorticity distributions in a cross-flow plane at $x/c = 0.80$ as shown in Figure 14 for $\alpha = 25^\circ$. Note that the results shown in this figure are phase-averaged over 30 cycles, and correspond to zero roll angle as the roll angle changes the sign from negative to positive. This is the reason for slight asymmetry, which is the result of the well-known hysteresis effect. It is seen that larger values of vorticity exist with increasing frequency. The variation of circulation with the

dimensionless frequency is shown in Figure 15. It is seen that the circulation of the vortical flow in a crossflow plane increases with frequency in comparison to the stationary wing.

IV. Conclusions

Passive lift enhancement for flexible nonslender delta wings has been demonstrated as a potential method for the control of vortex dominated wing flows. Physical mechanisms of lift enhancement and the effect of important variables have been discussed. Lift enhancement for flexible wings with low/moderate sweep is a very complex phenomenon. The generation of self-induced antisymmetric vibrations of leading edges is not completely understood, however it is certain that these vibrations produce the observed lift enhancement. The spanwise camber effect due to the large time-averaged deflection does not contribute at all. The main mechanism of lift enhancement is the excitation of shear layer instabilities and promotion of reattachment of the separated flow. There are substantial effects on the vortical flow with increasing wing flexibility, as the oscillating leading edge is an unsteady source of vorticity. The time-averaged vorticity flux increases due to the oscillating leading edge, which leads to increased circulation. Despite the increasing strength of the vortical flow, re-formation of the leading edge vortices with axial flow is observed, which suggests that the streamwise pressure gradient might be modified favorably due to the wing motion. The mean breakdown location becomes a maximum at an optimum frequency.

Acknowledgements

This work is supported by the European Office of Aerospace Research and Development, US Air Force Office of Scientific Research, Air Force Research Laboratory, under Contract No. F61775-02-C4024.

References

- ¹Taylor, G. and Gursul, I., "Lift Enhancement over a Flexible Delta Wing", AIAA-2004-2618, 2nd Flow Control Conference, 28 June-1 July 2004, Portland, Oregon.
- ²Taylor, G., Kroker, A. and Gursul, I., "Passive Flow Control over Flexible Nonslender Delta Wings", AIAA-2005-0865, 43rd Aerospace Sciences Meeting and Exhibit Conference, 10-13 January 2005, Reno, NV.
- ³Gursul, I., Survey Article: "Review of Unsteady Vortex Flows over Slender Delta Wings", *Journal of Aircraft*, in print.
- ⁴Traub, L. W., "Lift Prediction of Spanwise Cambered Delta Wings", *Journal of Aircraft*, Vol. 36, No. 3, pp. 515-522, May-June 1999.
- ⁵Taylor, G.S., Schnorbus, T., and Gursul, I., "An Investigation of Vortex Flows over Low Sweep Delta Wings", AIAA-2003-4021, AIAA Fluid Dynamics Conference, 23-26 June, Orlando, FL.
- ⁶Taylor, G. and Gursul, I., "Buffeting Flows over a Low Sweep Delta Wing", *AIAA Journal*, vol.42, no 9, September 2004, pp.1737-1745.
- ⁷Gordnier, R. E. and Visbal, M. R., "Higher-Order Compact Difference Scheme Applied to the Simulation of a Low Sweep Delta Wing Flow", AIAA 2003-0620, 41st AIAA Aerospace Sciences Meeting and Exhibit, 6-9 January 2003, Reno, NV.
- ⁸Roos, F.W. and Kegelman, J.T., "Control of Coherent Structures in Reattaching Laminar and Turbulent Shear Layers", *AIAA Journal*, vol. 24, no. 12, December 1986, pp. 1956-1963.

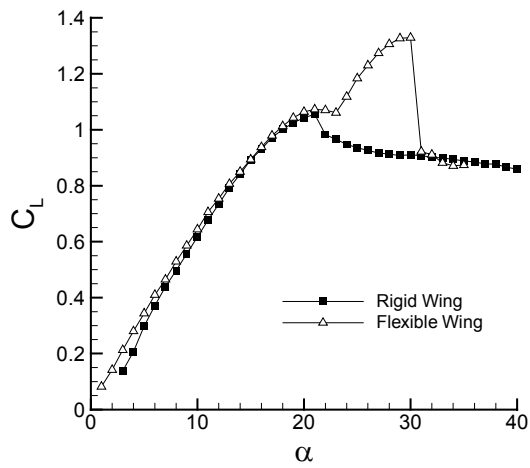


Figure 1: Variation of lift coefficient with incidence in wind tunnel experiments for a 50°-sweep angle delta wing.

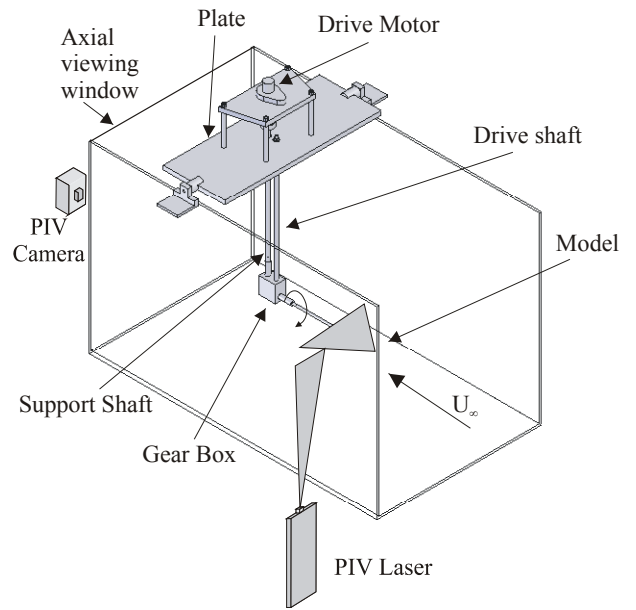


Figure 3: Overview of experimental setup in the water tunnel.

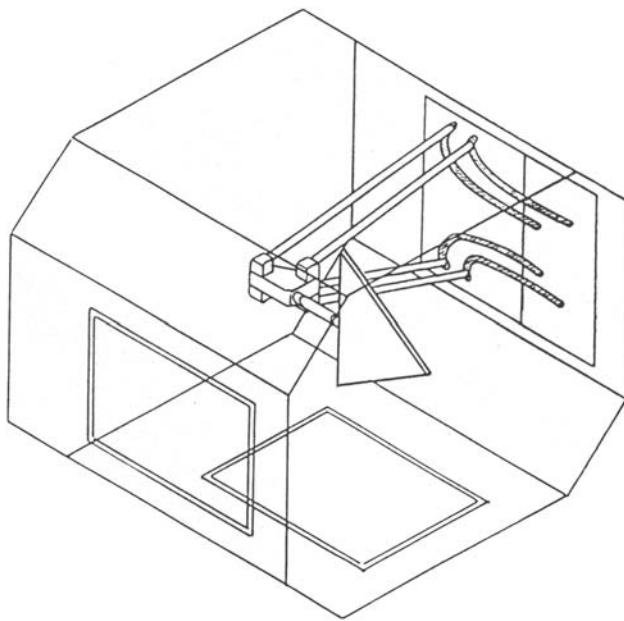


Figure 2: Schematic of the working section and high incidence rig, 7' x 5' wind tunnel, University of Bath.

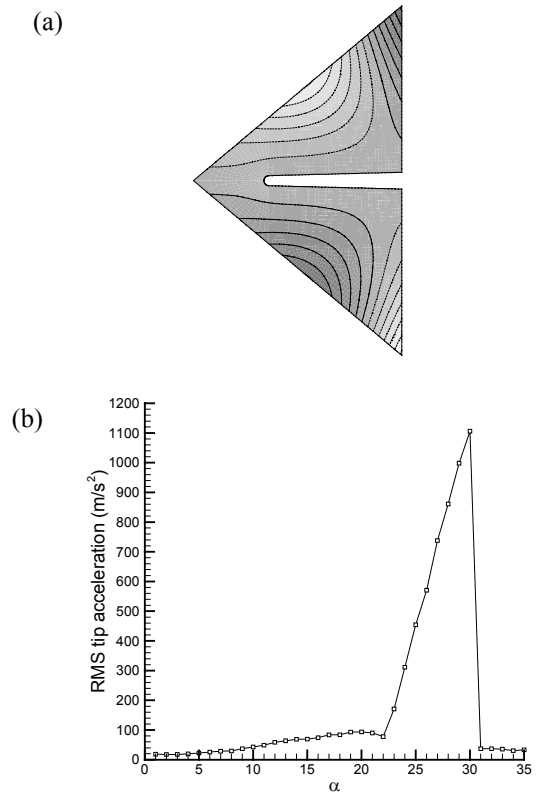


Figure 4: (a) Dominant anti-symmetric mode of vibration in wind tunnel experiments; (b) variation of root-mean-square of wing tip acceleration as a function

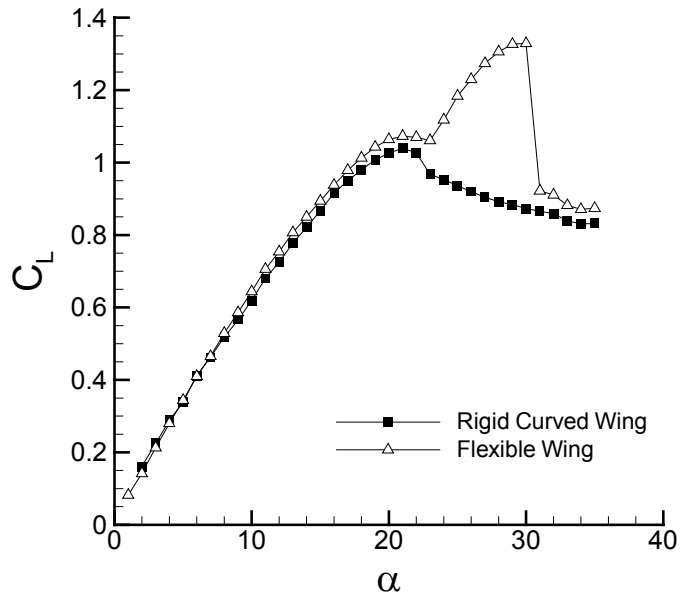


Figure 5: Variation of lift coefficient with incidence in wind tunnel experiments for flexible wing and rigid curved wing.

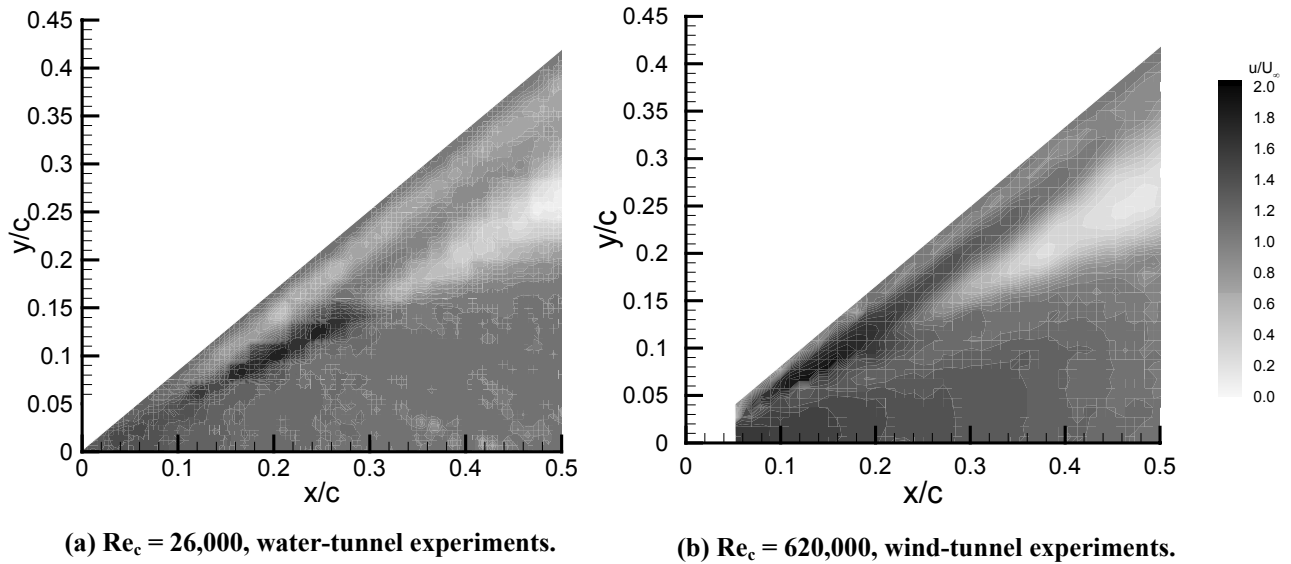
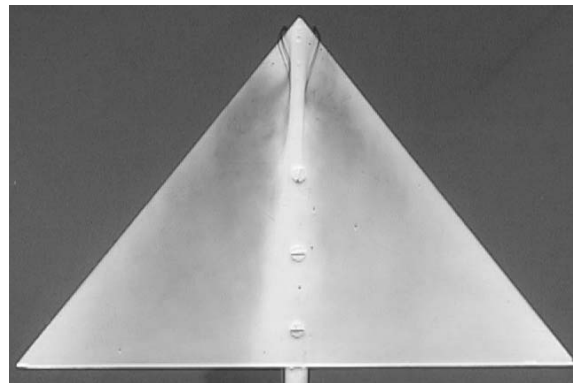
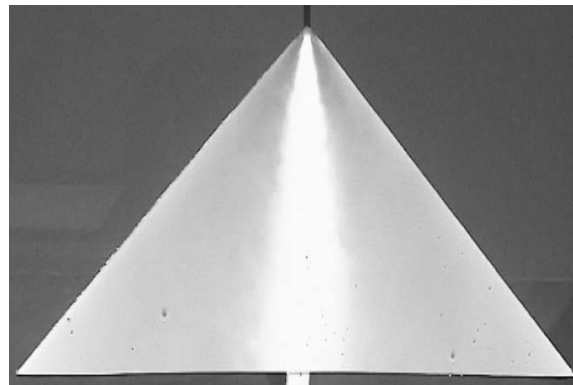


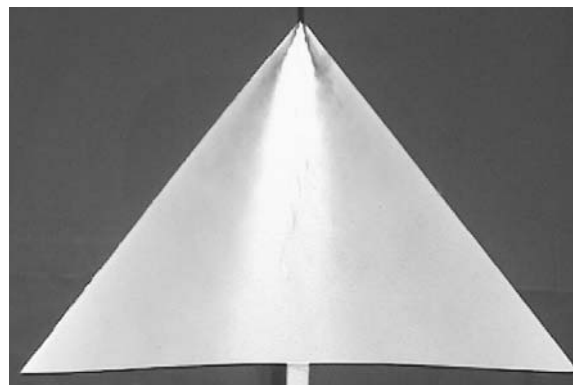
Figure 6: Contours of magnitude of time-averaged velocity in a plane through the vortex core in (a) water tunnel and (b) wind tunnel experiments, $\alpha = 15^\circ$.



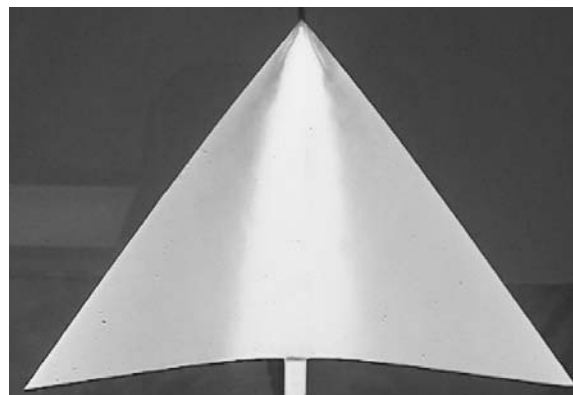
$\lambda = 0$



$\lambda = 2.35$



$\lambda = 5.56$



$\lambda = 21.28$

Figure 7: Flow visualization for rigid and flexible wings in water tunnel, $\alpha = 20^\circ$.

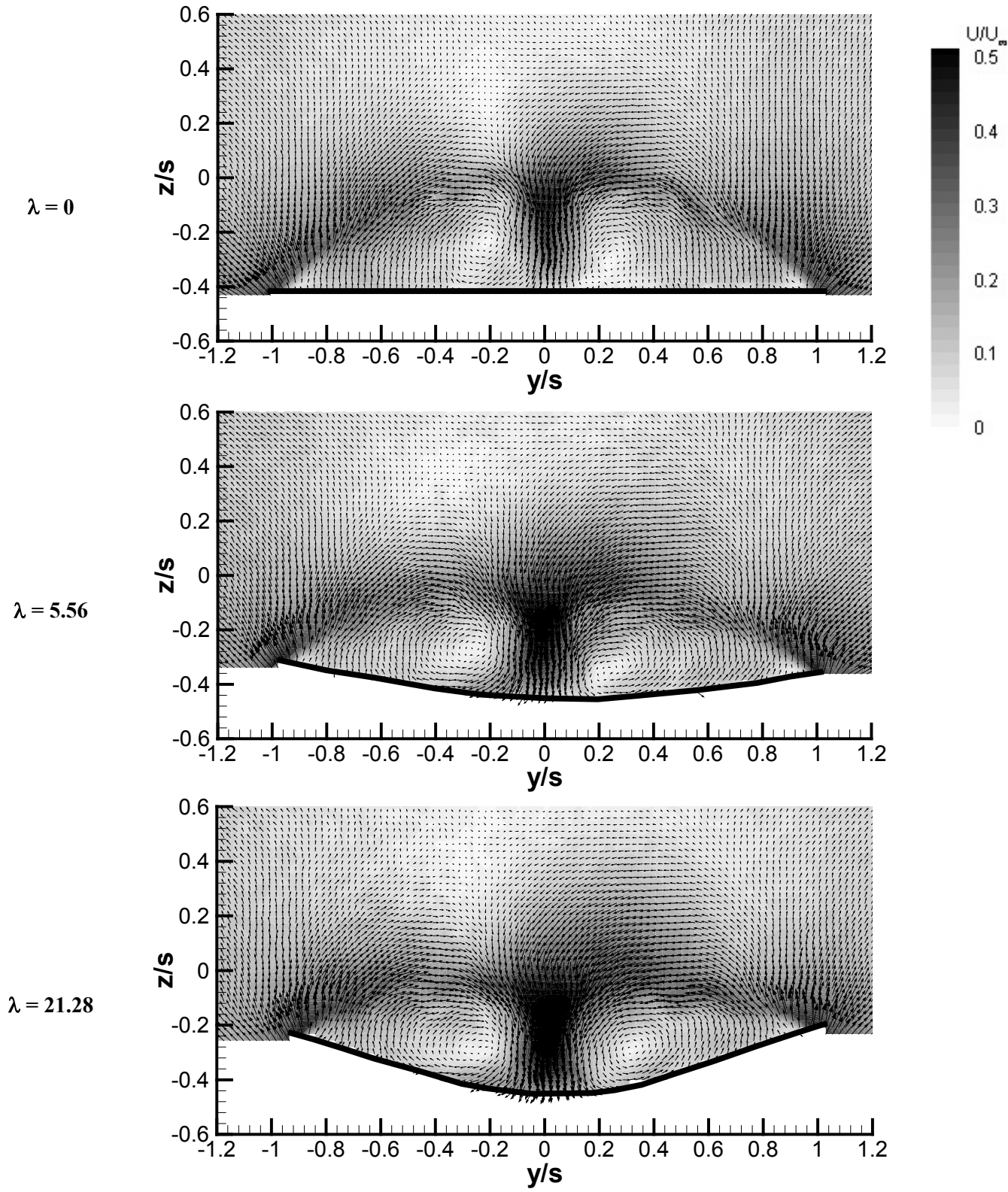


Figure 8: Vectors and contours of magnitude of time-averaged velocity in a cross-flow plane at $x/c=0.8$ for rigid and flexible wings in water tunnel experiments, $\alpha = 25^\circ$.

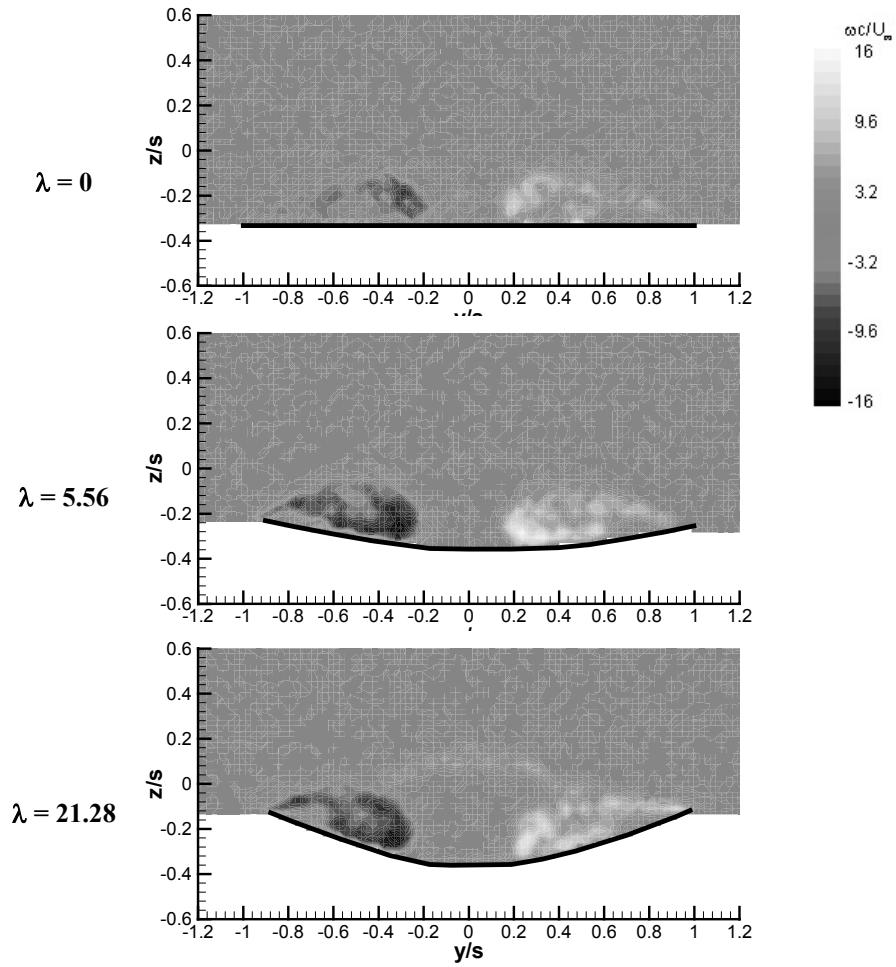


Figure 9: Magnitude of vorticity in a cross-flow plane at $x/c=0.8$ for rigid and flexible wings in water tunnel experiments, $\alpha = 20^\circ$.

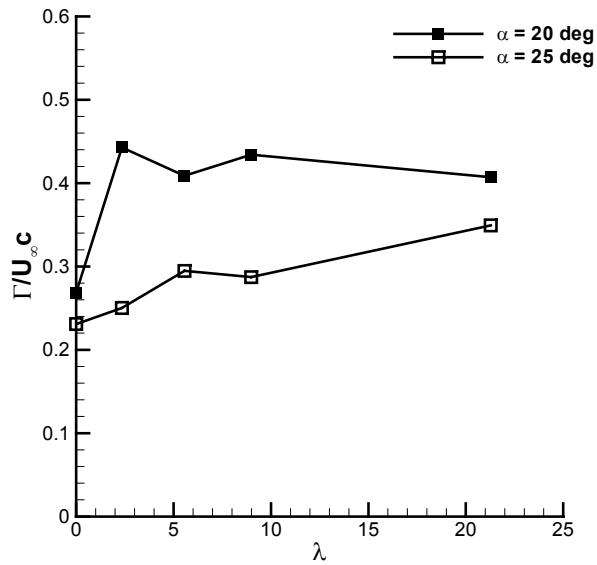
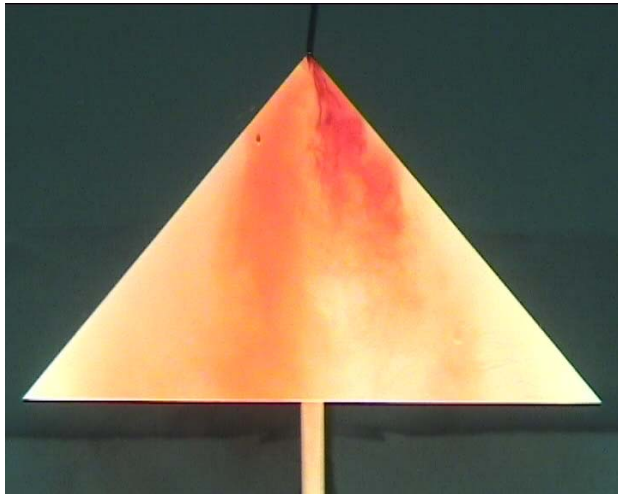
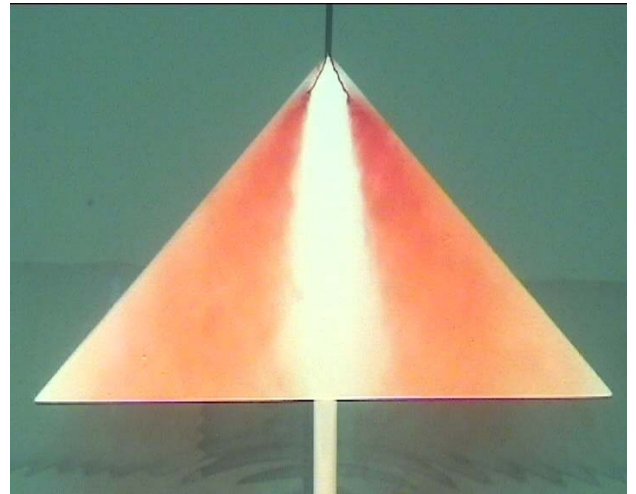


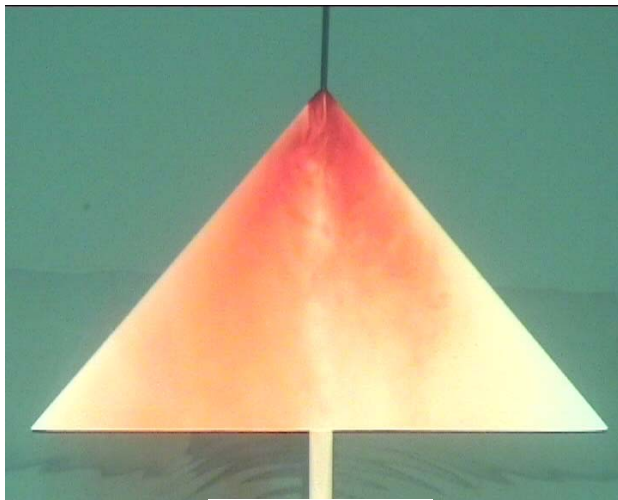
Figure 10: Variation of normalized circulation with wing flexibility.



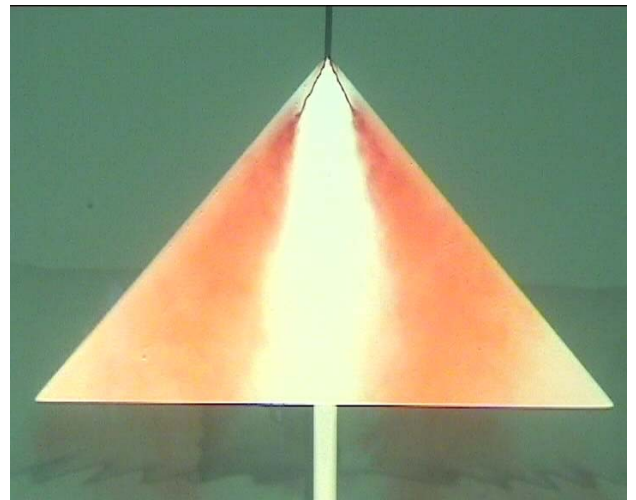
$fc/U_\infty = 0$



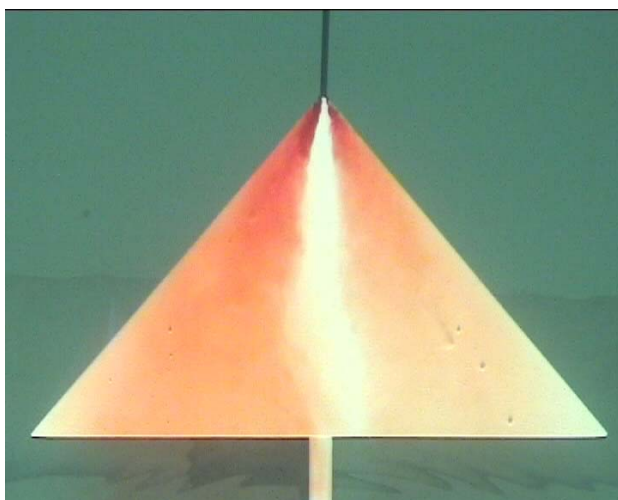
$fc/U_\infty = 0.5$



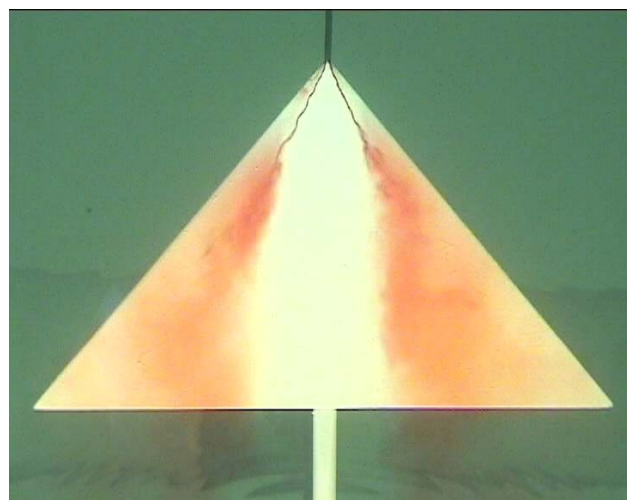
$fc/U_\infty = 0.15$



$fc/U_\infty = 0.89$



$fc/U_\infty = 0.3$



$fc/U_\infty = 1.78$

Figure 11: Flow visualization for a stationary and small-amplitude ($\phi=5^\circ$) rolling wing in water tunnel experiments.

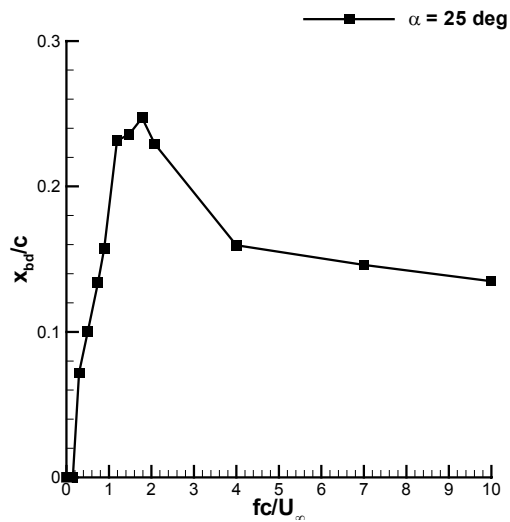
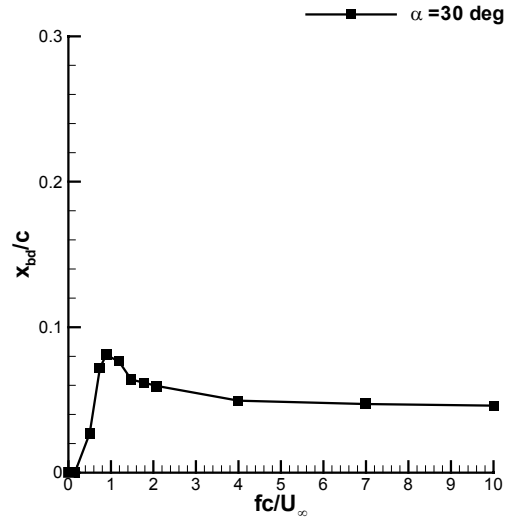
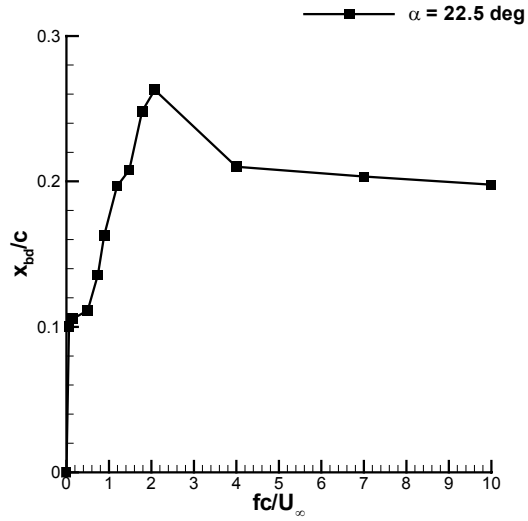
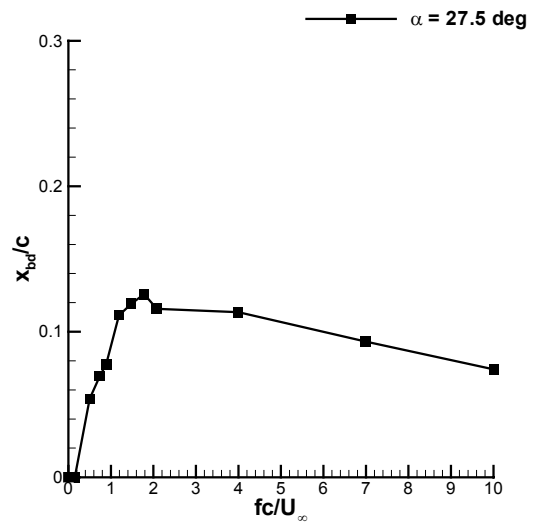
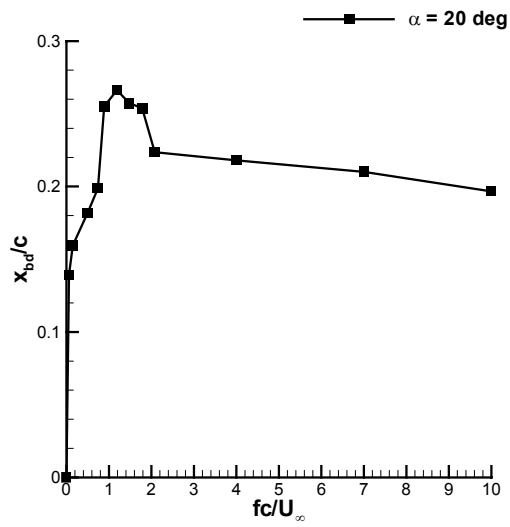


Figure 12: Variation of mean breakdown locat

on of dimensionless frequency for

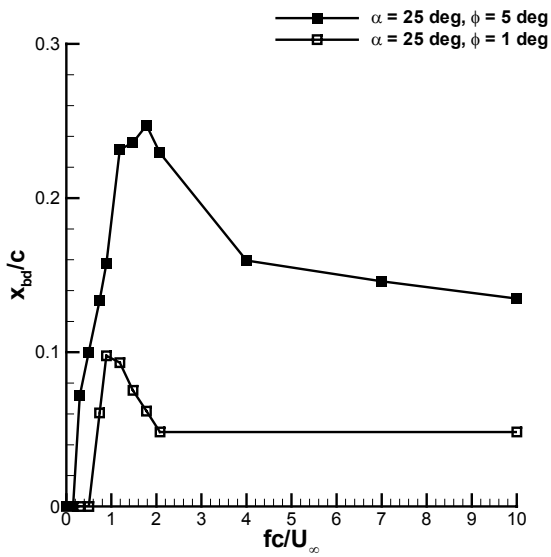


Figure 13: Variation of mean breakdown location as a function of dimensionless frequency for two values of rolling motion in water tunnel experiments, $\alpha=25^\circ$.

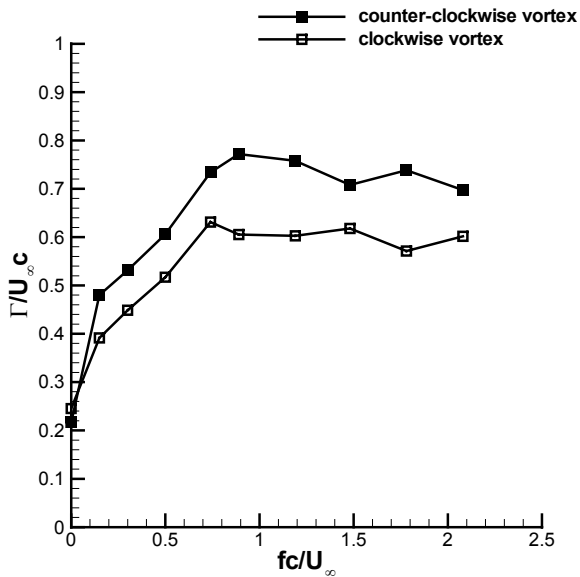


Figure 15: Variation of normalized circulation of vortical flow in a cross-flow plane at $x/c = 0.8$ as a function of dimensionless frequency in water tunnel experiments, $\alpha=25^\circ$.

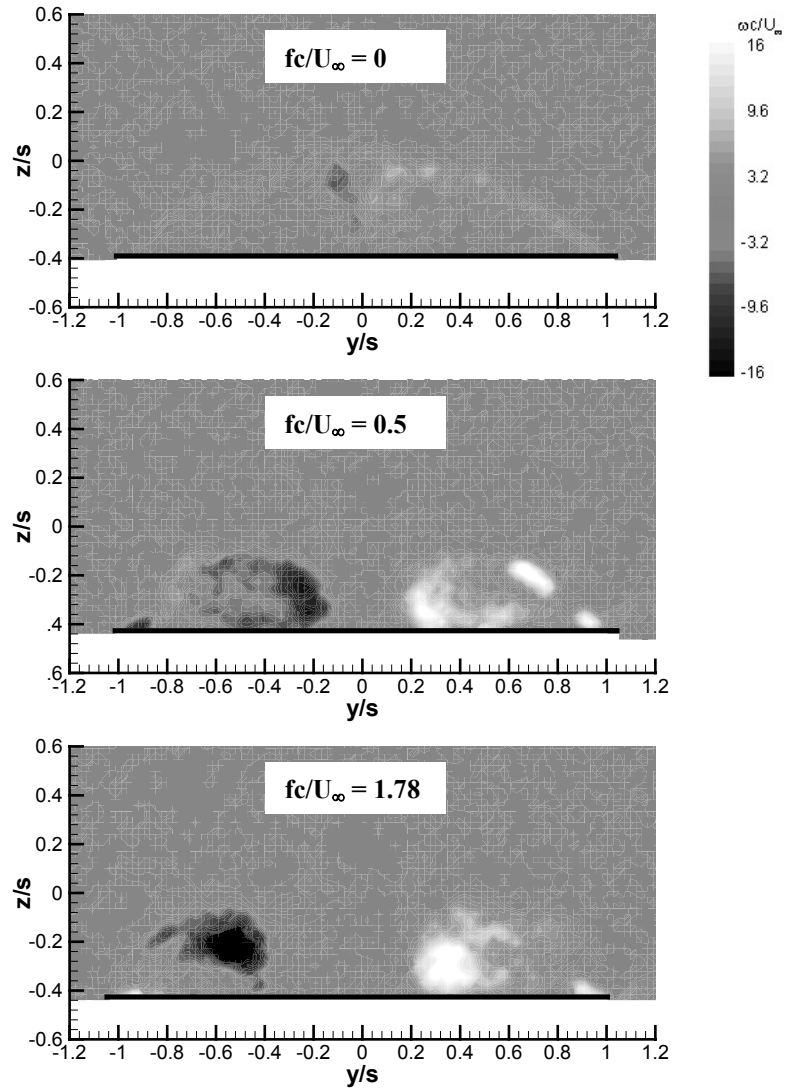


Figure 14: Magnitude of vorticity in a cross-flow plane at $x/c=0.8$ for stationary and rolling wings in water tunnel experiments, $\alpha = 25^\circ$.